ISSN 2715-4211

ASSET

Advance Sustainable Science, Engineering, and Technology

Available online at: publication.upgris.ac.id/index.php/asset/

Vol 1, No 1 (2019)

Advance Sustainable Science, Engineering and Technology (ASSET)

Volume 1 No. 1 2019

Editorial Board

Advance Sustainable Science, Engineering and Technology (ASSET)

Volume 1 No. 1 2019

Table of Content

First-Principles Calculation of Laser Crystal Multiplet Levels via Hybridized Density Functional Theory and Configuration Interaction within the OLCAO Method

Benjamin Walker

University of Missouri – Kansas City, 257 Flarsheim Hall, 5110 Rockhill Road, Kansas City, Missouri, 64110

baw5ea@mail.umkc.edu

Abstract. Computation of highly-localized multiplet energy levels of transition metal dopants is essential to the design of materials such as laser host crystals. A purely first-principles density functional theory-configuration interaction (DFT-CI) hybrid computational method has been developed to accurately compute multiplet energy levels for single atoms of carbon, nitrogen, oxygen, sodium, aluminum, silicon, titanium, and chromium. The multiplet energy levels have been computed with close experimental agreement in terms of magnitude and degeneracy, and the method does not depend on empirical information (i.e. Racah parameters). The computed multiplet energy level results are distributed according to term symbols, which are then compared to experimentally-observed multiplet energy levels. The hybrid method consists of analytic computation of two-electron integrals via the DFT-based orthogonalized linear combination of atomic orbitals (OLCAO) method, which are subsequently used as input for the CI-based discrete variational multi-electron (DVME) method to obtain the multiplet energy values.

Keywords: exchange-correlation; elecron repulsion integral; multiplet; DVME; OLCAO; density functional theory; configuration interaction

1. Introduction

A key driving economic force over the past few decades has been the development of advanced materials with novel and/or highly tuned properties. This trend is expected to continue into the future due to tough global competition for manufactured products, new technologies, and the demand for progress in fundamental science. Many manufactured products and new technologies rely heavily on subtle details of the electronic structures of the component materials. In order to achieve optimal performance within the constraints (e.g. thermal, mechanical, form factor, *etc*.) imposed by the specific application it is necessary to possess fundamental understanding of the material. A few general application examples include photovoltaics, laser host crystals, photo-detectors, lighting phosphors, and quantum dots [1–5]. Specific areas of fundamental physical importance are excitonic states, electron mobility, electron-phonon coupling, and precise band structure including multiplet and satellite energy levels [6–8]. These applications and points of fundamental research are intimately associated with excitations of the valence band electrons into the unoccupied conduction band states. Therefore, an area of particularly urgent research interest is the ability to make an accurate determination of the excited state properties of materials with an emphasis on those containing doped atoms with *3d*, *4d*, and *4f* valence electrons

because they tend to possess the most uniquely tunable properties. The presence of such dopant atoms within a solid introduces additional highly localized electronic states into the gap between the occupied and unoccupied states. Figure 1 shows a comparison between the band structures of undoped Al_2O_3 and chromium-doped Al_2O_3 (ruby).

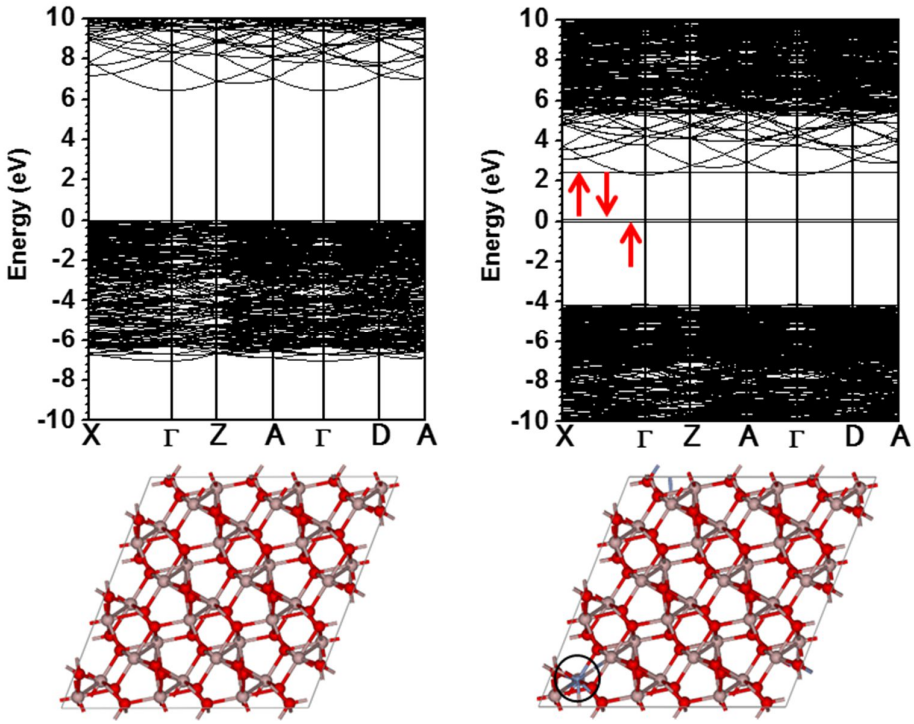

Figure 1. α-Al_2O_3 band structure example. α-Al_2O_3 with and without dopant. Left: Supercell band and crystal structure of α-Al_2O_3. Right: As the left side with a Cr substitutional defect (circled). Induced multiplet states are identified by arrows.

Experimental spectroscopic techniques to study these types of materials systems have progressed very far in recent decades, but it is clear that fundamental understanding and efficient analysis is only achieved when theoretical and computational methods are applied as well. In response to this need, tremendous effort has been expended to develop and apply such methods [9,10]. At present, computational theoretical methods have proven themselves to be extremely cost effective, efficient, and powerful tools. However, as with experiment, each computational method has its own set of advantages and disadvantages in terms of capability, accuracy, and efficiency. In fact, increased accuracy tends to come at the cost of efficiency, and vice versa. A prime example is that many methods need to explicitly compute the excited state electronic wave function for accurate prediction of the spectral properties of a material. Such an explicit wave function calculation has never been feasible for bulk solids due to the high computational cost involved; rather it has been used with smaller molecule-sized systems. While progress has been made, very substantial challenges remain in addressing these disadvantages and will likely require many more years of focused effort.

An example is the case of ruby; it has three lines (R, R', B) and three bands (U, Y, Y') in the visible spectrum which correspond to multiplets of impurity states. There have been studies that successfully computed multiplet levels from first principles. For example, Ohnishi and Sugano [11] computed two multiplet states of ruby, ^2E (R line) and $^4T_2$ (U band). In 1998 Prof. Ogasawara et al.[12] calculated the multiplet structure of ruby via a many-electron extension of the DV-Xα method [13] (Figure 2) thereby

elucidating the effects that covalency and trigonal distortion of the impurity-state wave function have on the multiplet structure of ruby.

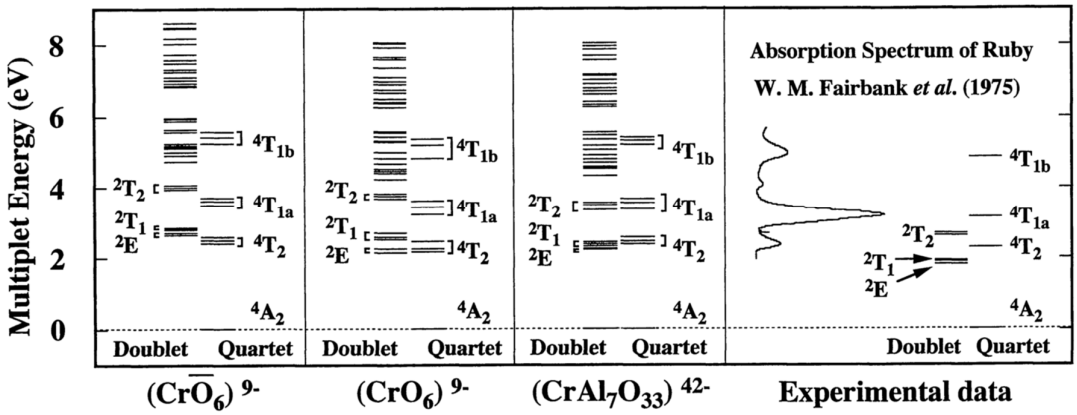

Figure 2. Ruby multiplet energy levels. Calculated multiplet energy levels of ruby using three different clusters, in comparison with the experimental absorption spectrum [14].

As is shown in Figure 2, there is a significant difference between the computed multiplet states of ruby, and those observed experimentally. For example, computed ^2E, $^2T_1$ and $^4T_2$ multiplet energy levels differ from their experimental counterparts in terms of quantity and magnitude. This difference is due to the presence of correlated electron-electron interactions that are not properly accounted for in the calculation.

The current state of the art in predicting laser crystal multiplet energy levels is to plot them with Tanabe-Sugano diagrams [15,16]. In this method, an approximation of the crystal field splitting energies as a function of ligand field strength is generated for tetrahedral or octahedral complexes. For instance, the *d*-orbital energy levels of neutral transition metals are degenerate, but in the presence of ligands the degeneracy of the energy levels is broken when crystal splitting occurs (denoted by Δ_{oct}).

Ruby is represented by an octahedral complex wherein a chromium atom is surrounded by six oxygen atoms. The energies of the $d_{xx\text{-}yy}$ and d_{zz} orbitals increase relative to those of the d_{xy}, d_{xz}, and d_{yz} orbitals. The energy splittings are characterized by empirically-determined Racah parameters [17] (denoted by *B* and *C*), which are meant to account for electron-electron repulsion. In this case, *B* represents the bond strength between the metal ion and the ligand, and is used to defined *C* as 1/4*B*. A Tanabe-Sugano diagram consists of the energy of an electron transition scaled by *B*, as a function of the crystal field splitting parameter Δ_{oct}, also scaled by *B*. While accurate, Tanabe-Sugano diagrams are dependent on empirically-derived Racah parameters. This work provides a framework for a method that is not dependent on the inclusion of empirical parameters to calculate multiplet energy levels. However, key challenges need to be addressed.

The essence of the problem being addressed in this work is that the excited state electronic properties of a solid can only be precisely described when correlated electron-electron interactions are taken into account. In strongly-correlated systems, atoms with partially occupied *d* and/or *f* electron shells exhibit atom-like behavior, thereby limiting the accuracy of the homogeneous electron gas model employed by LDA- and GGA-based methods. The situation becomes even more complicated when electrons are excited into higher energy levels, because the excitation changes the electronic structure of the entire system. Electron-electron interaction phenomena cannot be decoupled from each other, which precludes direct calculation of their effects. However, the effects can collectively be accounted for via the strategic application of suitable computational methods – in effect, a hybrid method.

2. Methods

2.1. DVME

The discrete variational multi-electron (DVME) method that is used for this work was developed in 2000 and has been successfully used to compute multiplet states for ruby [18-20]. In that work, an effective Hamiltonian was employed that takes only dopant-state electrons explicitly into account:

$$H = \sum_{i=1}^{M} h(\vec{r}_i) + \sum_i \sum_{j<i} g(\vec{r}_i, \vec{r}_j) \tag{1}$$

Here, $\vec{r}_i$ is the position of the i^{th} electron and M is the number of electrons occupying dopant states. The first term in the effective Hamiltonian is the one-electron operator:

$$h(\vec{r}) = -\frac{1}{2}\nabla^2 + V_{ext}(\vec{r}) + V_0(\vec{r}) \tag{2}$$

This is composed of the following terms: ∇^2 is the kinetic energy term, $V_{ext}(\vec{r})$ is the Coulombic potential from surrounding nuclei, and $V_0(\vec{r})$ is the Coulombic repulsion energy from the core and valence electrons. The second term in the effective Hamiltonian is the two-electron operator:

$$g(\vec{r}_i, \vec{r}_j) = \frac{1}{|\vec{r}_{ij}|} \tag{3}$$

where $\vec{r}_{ij}$ is the distance between the i^{th} and j^{th} impurity state electrons.

According to the prior work of Prof. Ogasawara, Slater determinants Φ_i, representing the impurity state orbitals, are constructed via the single-electron cluster calculation described in 2000[18]. Determination of the energy levels of the impurity states starts with diagonalizing the effective Hamiltonian within the subspace spanned by Φ_i. Next, the matrix elements of the Hamiltonian H are expanded to obtain:

$$H_{pq} = \langle \Phi_p | H | \Phi_q \rangle = \sum_{i=1}^{L}\sum_{j=1}^{L} A_{ij}^{pq} \langle i|h|j\rangle + \sum_{i=1}^{L}\sum_{j=1}^{L}\sum_{k=1}^{L}\sum_{\ell=1}^{L} B_{ijkl}^{pq} \langle ij|g|kl\rangle \tag{4}$$

where L is the number of impurity state orbitals, A and B are coefficients, and Φ_i are Slater determinants constructed from impurity state orbitals obtained from the CI cluster calculation. Additionally, $\langle i \mid h \mid j \rangle$ is the one-electron integral, and $\langle ij \mid g \mid kl \rangle$ is the two-electron integral, also known as the electron repulsion integral (ERI). These integrals are defined as follows:

$$\langle i|h|j\rangle = \int \phi_i^*(\vec{r}) h(\vec{r}) \phi_j(\vec{r}) d\vec{r} \tag{5}$$

$$\langle ij|g|kl\rangle = \int\int \phi_i^*(\vec{r}_1)\phi_j^*(\vec{r}_2)\frac{1}{|r_{12}|}\phi_k(\vec{r}_1)\phi_l(\vec{r}_2) d\vec{r}_1 d\vec{r}_2 \tag{6}$$

In these integrals, the ϕ terms represent impurity-state orbitals. Next, eigenvectors are obtained to express the many-electron impurity state wave function:

$$a_{n1}, a_{n2}, \cdots, a_{nK} \tag{7}$$

$$\Psi_n = a_{n1}\Phi_1 + a_{n2}\Phi_2 + \cdots + a_{nK}\Phi_K \tag{8}$$

where K is the number of Slater determinants. This is the CI formalism defined in the previous section. H is diagonalized in terms of Ψ_n to obtain the energy of the n^{th} eigenstate:

$$E^n = \left\langle \Psi_n \middle| H \middle| \Psi_n \right\rangle = \sum_p^K \sum_q^K a_{np}^* a_{nq} H_{pq} \tag{9}$$

A major distinction to be made between the DVME method as shown here and the work being presented in this dissertation is how the ERIs are computed. The stand-alone DVME method computes ERIs numerically[18] via random sampling points, a method that is less accurate than analytical computation; furthermore, it is and exceedingly expensive calculation for large systems. The hybrid DFT-CI method of this dissertation removes this complication by analytically computing the ERI solutions and substituting them into the effective Hamiltonian to be used in the aforementioned DVME procedure. The ERI derivation is shown in the subsequent section on interaction integrals.

The Hartree-Fock method and its derivatives rely on direct computation of the wave function of the system being studied. In the next section an alternative approach in the form of density function theory will be discussed, with subsequent discussion about how the hybrid DFT-CI method is formed.

2.2. Orthogonalized Linear Combination of Atomic Orbitals (OLCAO) Method

Over the past several decades, meeting the challenge of calculating the properties of materials has been made possible by the emergence of powerful and efficient computer and algorithms. The DFT-based OLCAO method [21] has been shown to be accurate and efficient for large periodic atomic systems [19,21]. The OLCAO method employs a basis of atom-centered atomic orbitals that are expanded as Gaussian functions, which facilitates accurate and efficient computation of interaction integrals.

Atomic Basis Functions

The solid state wave function $\Psi_{n\vec{k}}\left(\vec{r}\right)$ for energy band index n and wave vector $\vec{k}$ is defined as:

$$\Psi_{n\vec{k}}\left(\vec{r}\right) = \sum_{i,\gamma} C_{i\gamma}^n\left(\vec{k}\right) b_{i\gamma}\left(\vec{k},\vec{r}\right) \tag{10}$$

For the i^{th} aggregated quantum number (principle, angular momentum, and magnetic) and the γ^{th} atom in the cell. The Bloch sum $b_{i\gamma}\left(\vec{k},\vec{r}\right)$ is defined as:

$$b_{i\gamma}\left(\vec{k},\vec{r}\right) = \frac{1}{\sqrt{N}} \sum_{\upsilon} \exp\left[i\left(\vec{k}\cdot\vec{R}_\upsilon\right)\right] u_i\left(\vec{r}-\vec{R}_\upsilon-\vec{t}_\gamma\right) \tag{11}$$

where $\vec{R}_\upsilon$ is the lattice vector and $\vec{t}_\gamma$ is the position of the γ^{th} atom. The sum over υ of u_i represents an atom-centered linear combination of atomic orbitals. Each atomic orbital consists of a radial part and an angular part:

$$u_i\left(\vec{r}\right) = \left[\sum_{j=1}^N A_j r^l \exp\left(-\alpha_j r^2\right)\right] \cdot Y_l^m\left(\theta,\phi\right) \tag{12}$$

where l and m are angular momentum quantum numbers and A_j are expansion coefficients. The N decay factors α_j of the sum of Gaussian-type orbitals (GTOs) are selected by empirically choosing minimum and maximum values and then obtaining the rest via a geometric series between them. During an OLCAO calculation, the same set $\{\alpha_j\}$ is used for all the atoms of a given element, as well as for all the orbitals for a given quantum number i. In this way, the basis functions are element-specific and predetermined. Because of this, interaction integrals are computed and reused.

The OLCAO method is based on the local density approximation (LDA) of density functional theory (DFT). Next, the Kohn-Sham equation for a system of interacting particles is obtained:

$$\left[-\vec{\nabla}^2 + V_{e-n}\left(\vec{r}\right) + V_{e-e}\left(\vec{r}\right) + V_{XC}\left[\rho\left(\vec{r}\right)\right]\right]\Psi_{n\vec{k}}\left(\vec{r}\right) = E_{n\vec{k}}\Psi_{n\vec{k}}\left(\vec{r}\right) \tag{13}$$

where $V_{e-n}\left(\vec{r}\right)$ represents the electron-nuclear potential, $V_{e-e}\left(\vec{r}\right)$ represents the electron Coulombic potential, and $V_{XC}\left[\rho\left(\vec{r}\right)\right]$ represents the exchange-correlation (XC) potential energy. The XC potential has a functional relationship to the charge density $\rho\left(\vec{r}\right)$. Here, $\rho\left(\vec{r}\right)$ is the electron density over occupied states:

$$\rho\left(\vec{r}\right) = \sum_{occ}\left|\Psi_{n\vec{k}}\left(\vec{r}\right)\right|^2 \tag{14}$$

The total energy of the system is:

$$E_T = \sum_{n,\vec{k}}^{occ} E_n\left(\vec{k}\right) + \int \rho\left(\vec{r}\right)\left(\varepsilon_{XC} - V_{nuc-e} - \frac{V_{e-e}}{2}\right)d\vec{r} + \frac{1}{2}\sum_{\gamma,\delta}\frac{Z_\gamma Z_\delta}{\vec{R}_\gamma - \vec{R}_\delta} \tag{15}$$

The first term is the sum of energies over occupied one-electron bands; within the middle term: ε_{XC} is XC energy, V_{nuc-e} is nucleus-electron attraction energy, and $\frac{V_{e-e}}{2}$ is electron-electron repulsion energy; the last term is a sum of nucleus-nucleus repulsion energy over the lattice sites, where δ and γ are lattice sites and Z_δ and Z_γ are atomic numbers at lattice sites δ and γ.

Atom-Centered Potentional Functions

The real-space charge distribution $\rho_{cry}\left(\vec{r}\right)$ for an OLCAO calculation is defined as follows:

$$\rho_{cry}\left(\vec{r}\right) = \sum_A \rho_A\left(\vec{r} - \vec{t}_A\right) \tag{16}$$

where:

$$\rho_A\left(\vec{r}\right) = \sum_{j=1}^{N} B_j \exp\left(-\beta_j \vec{r}^2\right) \tag{17}$$

The atom-centered Coulomb potential $V_{Coul}\left(\vec{r}\right)$ is expressed as follows:

$$V_{Coul}\left(\vec{r}\right) = \sum_A V_C\left(\vec{r} - \vec{t}_A\right) \tag{18}$$

where $V_C\left(\vec{r}\right)$ is defined as

$$V_C\left(\vec{r}\right) = -\frac{Z_A}{\left|\vec{r}\right|}\exp\left(-\varsigma r^2\right) - \sum_{j=1}^{N} D_j \exp\left(-\beta_j \vec{r}^2\right) \tag{19}$$

The first term represents the electron-nuclear potential, where Z_A is the atomic number of the atom at the nucleus site; the second term of $V_C\left(\vec{r}\right)$ is the electron-electron potential.

The exchange-correlation potential $V_{XC}\left(\vec{r}\right)$ is defined as

$$V_{xc}\left(\vec{r}\right) = \sum_A V_x\left(\vec{r} - \vec{t}_A\right) \tag{20}$$

where:

$$V_x(\vec{r}) = \sum_{j=1}^{N} F_j \exp\left(-\beta_j \vec{r}^2\right) \tag{21}$$

The crystal potential is defined as a sum of the above atom-centered potentials:

$$V_{cry}(\vec{r}) = \sum_A V_A(\vec{r} - \vec{t}_A) \tag{22}$$

where:

$$V_A(\vec{r}) = V_C(\vec{r}) + V_x(\vec{r}) \tag{23}$$

The same set of exponential decay parameters $\{\beta_j\}$ is used in the above Gaussian functions. This allows for reuse of the expanded Gaussian functions $\exp\left(-\beta_j \vec{r}^2\right)$, hence fewer integral computations need to be performed. The mathematical form of $\rho_A(\vec{r})$ and $V_A(\vec{r})$ allows for the analytical computation of multicenter interaction integrals, which is a factor that lends to the computational efficiency of OLCAO.

Gaussian-Type Orbitals (GTOs)

Computation of symmetric band structure about the Brillouin zone is accomplished by solving the secular equation:

$$\left| H_{i\gamma,j\delta}(\vec{k}) - S_{i\gamma,j\delta}(\vec{k}) E(\vec{k}) \right| = 0 \tag{24}$$

where:

$$\begin{aligned} S_{i\gamma,j\delta}(\vec{k}) &= \left\langle b_{i\gamma}(\vec{k},\vec{r}) \,|\, b_{j\delta}(\vec{k},\vec{r}) \right\rangle \\ &= \sum_\mu \exp\left(-i\vec{k}\cdot\vec{R}_\mu\right) \int u_i(\vec{r} - \vec{t}_\gamma)\, u_j(\vec{r} - \vec{R}_\mu - \vec{t}_\delta) d\vec{r} \end{aligned} \tag{25}$$

and:

$$\begin{aligned} H_{i\gamma,j\delta}(\vec{k}) &= \left\langle b_{i\gamma}(\vec{k},\vec{r}) \,|\, H \,|\, b_{j\delta}(\vec{k},\vec{r}) \right\rangle \\ &= \sum_\mu \exp\left(-i\vec{k}\cdot\vec{R}_\mu\right) \int u_i(\vec{r} - \vec{t}_\gamma) \left[-\nabla^2 + V_{Coul}(\vec{r}) + V_{ex}(\vec{r}) \right] u_j(\vec{r} - \vec{R}_\mu - \vec{t}_\delta) d\vec{r} \end{aligned} \tag{26}$$

where $\vec{k}$ represents a set of ***k***-points. Even for larger systems of hundreds or thousands of atoms, the number of interaction integrals that need to be computed remains manageable due to the reuse of interaction integrals.

With the atom-centered potentials in-hand, let u_i be an s-type ($\ell = 0$) Gaussian function with decay parameter α_1, centered at atomic site *A*:

$$|\phi_A\rangle = \exp\left(-\alpha_1 \vec{r}_A^{\,2}\right) \tag{27}$$

where $\vec{r}_A = \vec{r} - \vec{A}$. OLCAO has a basis of Gaussian-type orbitals (GTOs), which is advantageous compared to other basis sets (i.e. plane wave basis). For example, a plane wave basis set requires many terms in order to accurately expand a wave function, making such bases more mathematically intense to compute. Gaussian functions are analytically integrated and differentiated easily.

Creating the OLCAO-DVME Hybrid Method

The first step in the hybrid calculation process is to accumulate the analytically computed single electron integrals and electron repulsion integrals with the OLCAO method. Single electron integrals consist of a sum of kinetic energy and nuclear attraction integral matrix elements. For the sake of brevity in describing the hybrid OLCAO-DVME method, single electron integrals and electron repulsion integrals are referred to as 'single integrals' and 'double integrals', respectively. To demonstrate how the single and double integrals are accumulated in OLCAO, the accumulation process for 2-center overlap integrals is shown here first.

Each atomic site has an atom-centered Gaussian function $|\phi_A\rangle = \exp\left(-\alpha_1 \vec{r}_A^{\,2}\right)$ with decay parameter α. Each alpha has a set of atomic orbitals (1s, 2s, $2p_x$, $2p_y$, $2p_z$, *etc*.), and the total number of valence orbitals for all the atoms in a given system is known as the valence dimension. When performing stand-alone OLCAO calculations, it is often preferable to consider only non-core electronic states. However, when preparing an OLCAO-DVME calculation, both core and valence orbitals are included in the single and double integrals.

In the case of 2-center overlap integrals, all pairs of alphas (without double counting) are tested for non-negligible Gaussian overlap (highlighted portion of the schematic of Figure 3.

	Atom 1						
Atom 2	α_{11}	α_{12}	α_{13}	α_{14}	α_{15}	α_{16}	α_{17}
	α_{21}	α_{22}	α_{23}	α_{24}	α_{25}	α_{26}	α_{27}
	α_{31}	α_{32}	α_{33}	α_{34}	α_{35}	α_{36}	α_{37}
	α_{41}	α_{42}	α_{43}	α_{44}	α_{45}	α_{46}	α_{47}
	α_{51}	α_{52}	α_{53}	α_{54}	α_{55}	α_{56}	α_{57}
	α_{61}	α_{62}	α_{63}	α_{64}	α_{65}	α_{66}	α_{67}
	α_{71}	α_{72}	α_{73}	α_{74}	α_{75}	α_{76}	α_{77}

Figure 3. Alpha pairs: highlighted are alphas involved in non-negligible overlap.

When this condition is met, the overlap integral subroutine is called for the alpha pair taking part in the non-negligible overlap. For each pair, the angular momentum character of the Gaussian function for the second alpha (α_2) determines the number of states over which the overlap is accumulated. This number is either 1, 4, 9, or 16 corresponding to *s*-, *p*-, *d*-, or *f*-type orbitals; this number is the upper bound on the accumulation loop. Starting from zero, each iteration of the loop adds the product of the orbital overlap of α_1 multiplied by each of the set of α_2. Once all the alphas are looped over, the integral with a complete basis representation is formed. This formalism is applied to 2-center overlap,

kinetic energy, 3-center electronic potential, and 3-center nuclear attraction integrals. Next, the single integrals are computed.

Single integrals are a term-by-term sum of the complete basis representation of kinetic energy and nuclear attraction integral matrix elements. The algorithm is as follows:

```
One(i,j) = 0
 do i=1,valeDim
  do j=1,valeDim
   One(i,j)=[KE(i,j)+NP(i,j)]
   write One(i,j)
  end do
 end do
```

The algorithm for double integrals is as follows:

```
Two(i,j,k,ℓ) = 0
do i=1,valeDim
 do j=1,valeDim
  do k=1,valeDim
   do ℓ=1,valeDim
    Two(i,j,k,ℓ)=ERI(i,j,k,ℓ)
    write Two(i,j,k,ℓ)
   end do
  end do
 end do
end do
```

The accumulated single and double integrals are used as input for DVME to perform a CI-style calculation that computes energy eigenvalues. It is important to note that the nuclear attraction integral within DVME treats the nucleus site as a point charge, whereas the nucleus site is treated with an *s*-type Gaussian function in OLCAO. Therefore, OLCAO-generated nuclear attraction integrals for use in the hybrid method are prepared in the DVME style. This means that the application of the Gaussian Product Theorem and factoring of constants is the same as for the 2-center overlap integral.

3. Results and discussion

The main result of this work is the development of a purely first-principles method for computing the multiplet energy levels of single atoms, specifically transition metal dopants within crystalline systems. Such a method has remained elusive due to the reduced accuracy of DFT-based methods when applied to strongly correlated systems, as well as the prohibitive computational expense in applying post-HF methods to periodic crystals. However, strategic application of both methods at different stages of a hybrid-style calculation has shown promising results.

The method computes atomic energy levels within the ground-state electron configuration. The multiplet energy values for atoms are distributed according to term symbols that have the form ${}^{2S+1}L_J$,

where S is the total spin quantum number, L is the total orbital quantum number, and J is the total angular momentum quantum number [22]. For a given pair of electrons within a subshell, we know that $L=\left|\ell_1-\ell_2\right|$ to $\ell_1+\ell_2$, $S=\left|s_1-s_2\right|$ to s_1+s_2, and $J=\left|L-S\right|$ to $L+S$. The value of L determines the letter code of the term symbol, such that $L=0$ corresponds to S, $L=1$ corresponds to P, *etc*. in the same way as orbitals are designated. Spin degeneracy is determined from the fact that each level has $2S+1$ states. One additional constraint is that the many-electron wave function must be anti-symmetric when considering the combination of spin and orbital angular momenta.

Putting this formalism into practice for Sodium, the single unpaired electron in the 3s subshell allows for straightforward tabulation of the ground-state term symbols. We have $S=\frac{1}{2}$, $L=0$, and $J=\frac{1}{2}$; this means we expect that there is a single anti-symmetric term $^2S_{1/2}$ for ground-state Sodium, with this state being doubly spin degenerate (containing $2S+1=2\left(\frac{1}{2}\right)+1=2$ states). This is in agreement with what has been observed experimentally [23], and is summarized in Table 1:

Table 1. Sodium multiplet energies (eV)

Term Symbol	OLCAO-DVME Method	DVME	Term Symbol	Experiment[23]
$^2S_{1/2}$	0.0000000	0.0000000	$^2S_{1/2}$	0.0000000

The next set of tables shows multiplet energy comparisons for carbon, nitrogen, oxygen, aluminum, silicon, titanium, and chromium.

Table 2. Carbon multiplet energies (eV)

Term Symbol	OLCAO-DVME Method	DVME	Term Symbol	Experiment [24]
$^3P_{0,1,2}$	0.000000	0.000000	$^3P_0$	0.0000000
	0.000000	0.000592	$^3P_1$	0.002035413
	0.000000	0.001132	$^3P_2$	0.005382583
$^1D_2$	1.506279	1.947265	$^1D_2$	1.263728
	1.506279	1.948595		
	1.506279	1.948948		
	1.506279	1.949887		
	1.506279	1.951090		
$^1S_0$	3.765696	4.8720310	$^1S_0$	2.684014

For carbon, there are three low energy term symbols that may be obtained via transition from the $[He]2s^22p^2$ ground state: ^3P, ^1D, and ^1S. Again, the superscript defines the spin configuration for each term symbol, and the number of energy values for each term symbol letter is determined by the number of orbitals of the same angular momentum combined with the anti-symmetric requirement. For instance, ^3P (read as 'triplet P') has three J values shown due to the possible allowed combinations of electron spin and orbital angular momenta that lead to anti-symmetric wave functions. Specifically, the ^3P has two parallel (symmetric) spins for a total S equal to one. Each electron has an orbital angular momentum

of one such that the total L may take on values of 2, 1, or 0. Consequently, based only on the addition of angular momentum via LS coupling, the possible J values are 3, 2, 1, or 0. Further refining this list to produce only anti-symmetric configurations leads to $S=1$, $L=1$ so that $J=2,1,0$.

The energetic differences among the ^{3}P states that are expressed in the NIST data are the result of spin-orbit coupling while the differences in the pure DVME data are the result of integration error. For the $^1D_2$ case the energy levels should possess orbital degeneracy and so only one is listed in the NIST data. As with the ^{3}P case, the energy differences in the stand-alone DVME results are due to integration error. This may be contrasted with the hybrid OLCAO-DVME results which show perfect degeneracy for all five orbitals.

The trends for atomic C continue with the other elements. Orbital degeneracies that are not due to spin-orbit coupling are exactly represented in the OLCAO-DVME method but not the stand-alone DVME method. Orbital degeneracies in the NIST data are reflected by only one number, but spin-orbit splittings are shown. There are some further anomalies that appear for higher Z atoms which will be discussed next.

Table 3. Nitrogen multiplet energies (eV)

Term Symbol	OLCAO-DVME Method	DVME	Term Symbol	Experiment[24]
$^4S_{3/2}$	0.000000	0.000000	$^4S_{3/2}$	0.000000
$^2D_{5/2,3/2}$	2.706276	3.199266	$^2D_{5/2}$	2.383523
	2.706276	3.199597	$^2D_{3/2}$	2.384610
	2.706276	3.201109		
	2.706276	3.201610		
	2.706276	3.203819		
$^2P_{1/2,3/2}$	4.510460	5.334013	$^2P_{1/2}$	3.575570
	4.510460	5.334013	$^2P_{3/2}$	3.575618
	4.510460	5.334790		

Table 4. Oxygen multiplet energies (eV)

Term Symbol	OLCAO-DVME Method	DVME	Term Symbol	Experiment[24]
$^3P_{0,1,2}$	0.000000	0.000000	$^3P_0$	0.000000
	0.000000	0.003016	$^3P_1$	0.019622
	0.000000	0.003738	$^3P_2$	0.028142
$^1D_2$	2.109835	2.346584	$^1D_2$	1.967364
	2.109835	2.351542		
	2.109835	2.352462		
	2.109835	2.353076		
	2.109835	2.355483		
$^1S_0$	5.274588	5.876203	$^1S_0$	4.189746

Table 5. Aluminum multiplet energies (eV)

Term Symbol	OLCAO-DVME Method	DVME	Term Symbol	Experiment [25,26]
$^2P_{1/2,3/2}$	0.000000	0.000000	$^2P_{1/2}$	0.000000
	0.000000	0.001079	$^2P_{3/2}$	0.013894
	0.000000	0.002662		

Table 6. Silicon multiplet energies (eV)

Term Symbol	OLCAO-DVME Method	DVME	Term Symbol	Experiment [27]
$^3P_{0,1,2}$	0.000000	0.000000	$^3P_0$	0.000000
	0.000000	0.000540	$^3P_1$	0.009561
	0.000000	0.002883	$^3P_2$	0.027668
$^1D_2$	1.126786	1.477118	$^1D_2$	0.780958
	1.126786	1.479868		
	1.126786	1.480659		
	1.126786	1.481468		
	1.126786	1.483393		
$^1S_0$	2.816966	3.699545	$^1S_0$	1.908659

Table 7. Titanium multiplet energies (eV)

Term Symbol	OLCAO-DVME Method	DVME	Term Symbol	Experiment [28]
$^3F_{2,3,4}$	0.000000	0	$^3F_2$	0.000000
	0.000000	0.00623	$^3F_3$	0.021094
	0.000000	0.00741	$^3F_4$	0.047967
	0.000000	0.01103		
	0.000000	0.01238		
	0.000000	0.02707		
	0.000010	0.02917		
$^5F_{1,2,3,4,5}$	0.895369	0.41582	$^5F_1$	0.8129437
	0.895380	0.41729	$^5F_2$	0.8181426
	0.895380	0.43587	$^5F_3$	0.82585948
	0.895380	0.43665	$^5F_4$	0.83599519
	0.895390	0.43999	$^5F_5$	0.8484192
	0.895390	0.44031		
	0.895390	0.44827		
$^1D_2$	1.13099	1.61907	$^1D_2$	0.8995494
	1.13099	1.62392		
	1.13099	1.62488		
	1.13099	1.69335		
	1.13099	1.70036		
$^3P_{0,1,2}$	1.32576	1.70226	$^3P_0$	1.0460073
	1.32576	1.70889	$^3P_1$	1.05292613
	1.32576	1.71082	$^3P_2$	1.06655473
$^3F_{2,3,4}$	-	-	$^3F_2$	1.42975613
	-	-	$^3F_3$	1.44315261
	-	-	$^3F_4$	1.46013858
	-	-		
	-	-		
	-	-		
	-	-		
$^1G_4$	1.78897	1.79972	$^1G_4$	1.5024892
	1.78897	1.81572		
	1.78897	1.8181		
	1.78898	2.0627		
	1.78898	2.06429		
	1.78898	2.06667		
	1.78898	2.067		
	1.78898	2.0705		
	1.78898	2.07094		
$^5P_{1,2,3}$	-	-	$^5P_1$	1.7335189
	-	-	$^5P_2$	1.7393044
	-	-	$^5P_3$	1.7488757

Table 8. Chromium multiplet energies (eV)

Term Symbol	OLCAO-DVME Method	DVME	Term Symbol	Experiment [29]
$^7S_3$	0.000000	0.000000	$^7S_3$	0.000000
$^5S_2$	2.11166	2.60561	$^5S_2$	0.941430
$^5D_{0,1,2,3,4}$	-	-	$^5D_0$	0.96097008
	-	-	$^5D_1$	0.96841323
	-	-	$^5D_2$	0.98287741
	-	-	$^5D_3$	1.00367492
	-	-	$^5D_4$	1.03000806
$^5G_{2,6,3,4,5}$	3.23514	2.69414	$^5G_2$	2.543836
	3.23514	2.69571	$^5G_6$	2.544100
	3.23514	2.70899	$^5G_3$	2.544268
	3.23514	2.71366	$^5G_4$	2.544606
	3.23514	2.72786	$^5G_5$	2.544639
	3.23514	3.82348		
	3.23514	3.82364		
	3.23514	3.82457		
	3.23514	3.82532		
$^5P_{3,2,1}$	3.66658	3.82683	$^5P_3$	2.707915
	3.66658	3.82789	$^5P_2$	2.708786
	3.66658	3.82918	$^5P_1$	2.709914
$^3P_{0,1,2}$	-	-	$^3P_0$	2.87187330
	-	-	$^3P_1$	2.91511321
	-	-	$^3P_2$	2.98716592
$^7P^o_{2,3,4}$	-	-	$^7P^o_2$	2.88945204
	-	-	$^7P^o_3$	2.89953683
	-	-	$^7P^o_4$	2.91348179
$^3H_{4,5,6}$	-	-	$^3H_4$	2.96741994
	-	-	$^3H_5$	2.98256886
	-	-	$^3H_6$	3.00044213
$^5D_{0,4,1,2,3}$	3.78868	3.83034	$^5D_0$	3.00997113
	3.78868	3.83181	$^5D_4$	3.01062750
	3.78868	4.34235	$^5D_1$	3.01114739
	3.78868	4.34514	$^5D_2$	3.01279639
	3.78868	4.34819	$^5D_3$	3.01329984

In each case shown, multiplet energies from the hybrid method match experimental values more closely than do their DVME counterparts, in terms of magnitude and degeneracy. Whereas the term symbols for a carbon atom are relatively straightforward to tabulate, the production of term symbols for higher-Z atoms like titanium and chromium is extremely complicated. However, the general rules explained above can be extended to treat generation higher-Z atoms [30].

Both sets of calculations (OLCAO-DVME hybrid method and stand-alone DVME method) were non-relativistic, so spin-orbit coupling was not taken into account. This explains why the experimental multiplet energy values are resolved according to individual term symbols (with differing magnitudes), and the multiplet energy values computed via the hybrid method are the same for a given term symbol letter. The improved agreement with respect to magnitude and degeneracy is a significant step forward because it demonstrates that the basic approach is sound and that additional improvements should be possible with the inclusion of higher-order theory. However, the above results also reveal limitations in the approach that will require further investigation before they can be fully resolved.

The multiplet energies shown for titanium and chromium are a subset of the total list of values produced; the hybrid method produced 225 multiplet energy values for titanium, and 400 for chromium. The full list of multiplet energy values for titanium and chromium is contained in an external appendix that is available with this document. The multiplet energy values shown for titanium and chromium convey that the hybrid method is capable of producing some of the multiplet energies with expected degeneracies and magnitudes, compared to experimental values. However, the method is insufficient to produce all the experimentally observed excited-state multiplets. The Cr $^5D_{0,1,2,3,4}$ (quintuplet D) state is not reproduced in the correct energetic order by either the stand-alone DVME method or the hybrid OLCAO-DVME method. The energy levels *are* computed (and can be seen in the full list of energy levels in the supplementary appendix available with this document), but their energies are much higher than experiment indicates. The precise reason for this discrepancy is unknown, but because the problem manifests itself primarily with configurations that include a significant *4s* orbital component it may be surmised that the basis function for that orbital is less than ideal. Likely, it is too compact. The effect of a compact orbital is to force the 4s electronic states to be too close to other orbitals, thus raising their energy primarily through Coulombic repulsion.

4. Conclusion

The application of the DFT-CI hybrid method related in this dissertation has yielded promising results evidenced by the experimentally accurate atomic energy levels shown the preceding calculations. Although the energy levels of single atoms have been accurately computed before with tools like GRASP2K [31,32], and the computation of multiplet energy levels of multi-atom clusters has also been possible, the important contribution of the formalism exhibited here is that it is extendable to treat multi-atom solids. Therefore, a major advance from this work is that a door is now opened to the computation of multiplet energy levels of wave functions that are expressed in terms of Bloch waves instead of just atomic orbitals or molecular orbitals as found in most other methods. Along the way, re-derivation of the existing interaction integrals in the OLCAO package has led to increased accuracy. For example, re-deriving the momentum matrix integrals rectified a long-standing problem that hampered the computation of the dielectric function and energy-loss function of high-Z atom containing materials.

Acknowledgements

I wish to express gratitude to my advisor, Dr. Paul Rulis. His patience, support, and encouragement have been an essential part of my work. A very special thanks to Dr. Kazuyoshi Ogaswara of Kwansei Gakuin University; his research experience and zeal have inspired me.

References

[1] Zunger, A., Wagner, S. & Petroff, P. M. New Materials and Structures for Photovoltaics. J. Electron. Mater. 22, 3–16 (1993).
[2] Atherton, L. J., Payne, S. A. & Brandle, C. D. Oxide and Fluoride Laser Crystals. Annu. Rev. Mater. Sci. 23, 453–502 (1993).
[3] Antoni, R. Heterostructure Infrared Photovoltaic Detectors. Infrared Phys. Technol. 41, 213–238 (2000).
[4] Lin, C. C. & Liu, R.-S. Advances in Phosphors for Light-emitting Diodes. J. Phys. Chem. Lett. 2, 1268–1277 (2011).
[5] Ramsay, A. J. A Review of the Coherent Optical Control of the Exciton and Spin States of Semiconductor Quantum Dots. Semicond. Sci. Technol. 25, 103001 (2010).
[6] Cocoletzi, G. H. & Mochán, W. L. Excitons: From Excitations at Surfaces to Confinement in Nanostructures. Surf. Sci. Rep. 57, 1–58 (2005).
[7] Buse. Light-Induced Charge Transport Processes in Photorefractive Crystals I: Models and Experimental Methods. Appl. Phys. B Lasers Opt. 64, 273–291 (1997).
[8] Shen, Z.-X. & Dessau, D. S. Electronic Structure and Photoemission Studies of Late Transition-

Metal Oxides — Mott Insulators and High-Temperature Superconductors. Phys. Rep. 253, 1–162 (1995).
[9] Huang, P. & Carter, E. A. Advances in Correlated Electronic Structure Methods for Solids, Surfaces, and Nanostructures. Annu. Rev. Phys. Chem. 59, 261–290 (2008).
[10] Klepeis, J. E. Introduction to First-Principles Electronic Structure Methods: Application to Actinide Materials. J. Mater. Res. 21, 2979–2985 (2006).
[11] Ohnishi, S. & Sugano, S. Theoretical Studies of High-Pressure Effects on Optical Properties of Ruby. Jpn. J. Appl. Phys. 21, L309–L311 (1982).
[12] Ogasawara, K. et al. Analysis of Covalent Effects on the Multiplet Structure of Ruby Based on First-Principles Cluster Calculations. Jpn. J. Appl. Phys. 37, 4590–4594 (1998).
[13] Tomohiko Ishii, Hisanobu Wakita, Kazuyoshi Ogasawara, & Yang-Soo Kim. The DV-Xα Molecular-Orbital Calculation Method. (Springer International Publishing, 2015).
[14] Fairbank, W. M., Klauminzer, G. K. & Schawlow, A. L. Excited-State Absorption in Ruby, Emerald, and MgO:Cr3+. Phys. Rev. B 11, 60–76 (1975).
[15] Tanabe, Y. & Sugano, S. On the Absorption Spectra of Complex Ions. I. J. Phys. Soc. Jpn. 9, 753–766 (1954).
[16] Tanabe, Y. & Sugano, S. On the Absorption Spectra of Complex Ions II. J. Phys. Soc. Jpn. 9, 766–779 (1954).
[17] Multiplets of Transition-Metal Ions in Crystals - 1st Edition. Available at: https://www.elsevier.com/books/multiplets-of-transition-metal-ions-in-crystals/sugano/978-0-12-676050-7. (Accessed: 14th December 2017)
[18] Ogasawara, K., Ishii, T., Tanaka, I. & Adachi, H. Calculation of Multiplet Structures of Cr^{3+} and V^{3+} in α-Al_2O_3 Based on a Hybrid Method of Density-Functional Theory and the Configuration Interaction. *Phys. Rev. B* **61,** 143 (2000).
[19] Ching, W. Y. Theoretical Studies of the Electronic Properties of Ceramic Materials. *J. Am. Ceram. Soc.* **73,** 3135–3160 (1990).
[20] Ogasawara, K. & Watanabe, S. Chapter 22 Current Situation and Future Development of Discrete Variational Multielectron Method. in *Advances in Quantum Chemistry* **Volume 54,** 297–314 (Academic Press, 2008).
[21] Ching, W.-Y. & Rulis, P. *Electronic Structure Methods for Complex Materials: The Orthogonalized Linear Combination of Atomic Orbitals*. (Oxford University Press, USA, 2012).
[22] Griffiths, D. J. *Introduction to Quantum Mechanics*. (Pearson Prentice Hall, 2004).
[23] Sansonetti, J. E. Wavelengths, Transition Probabilities, and Energy Levels for the Spectra of Sodium (NaI–NaXI). *J. Phys. Chem. Ref. Data* **37,** 1659–1763 (2008).
[24] Tables of Spectra of Hydrogen, Carbon, Nitrogen, and Oxygen Atoms and Ions. *CRC Press* (1993). Available at: https://www.crcpress.com/Tables-of-Spectra-of-Hydrogen-Carbon-Nitrogen-and-Oxygen-Atoms-and-Ions/Gallagher-Moore/p/book/9780849374203. (Accessed: 9th August 2017)
[25] Martin, W. C. & Zalubas, R. Energy levels of aluminum, Al I through Al XIII. *J. Phys. Chem. Ref. Data* **8,** 817–864 (1979).
[26] Kaufman, V. & Martin, W. C. Wavelengths and Energy Level Classifications for the Spectra of Aluminum (Al I through Al XIII). *J. Phys. Chem. Ref. Data* **20,** 775–858 (1991).
[27] Martin, W. C. & Zalubas, R. Energy Levels of Silicon, Si I through Si XIV. *J. Phys. Chem. Ref. Data* **12,** 323–380 (1983).
[28] Saloman, E. B. Energy Levels and Observed Spectral Lines of Neutral and Singly Ionized Titanium, Ti I and Ti II. *J. Phys. Chem. Ref. Data* **41,** 013101-013101-116 (2012).
[29] Saloman, E. B. Energy Levels and Observed Spectral Lines of Neutral and Singly Ionized Chromium, Cr I and Cr II. *J. Phys. Chem. Ref. Data* **41,** 043103 (2012).
[30] Hyde, K. E. Methods for Obtaining Russell-Saunders Term Symbols from Electronic Configurations. *J. Chem. Educ.* **52,** 87 (1975).
[31] Jönsson, P., He, X., Froese Fischer, C. & Grant, I. P. The grasp2K Relativistic Atomic Structure Package. *Comput. Phys. Commun.* **177,** 597–622 (2007).

[32] Jönsson, P., Li, J., Gaigalas, G. & Dong, C. Hyperfine Structures, Isotope Shifts, and Transition Rates of C II, N III, and O IV from Relativistic Configuration Interaction Calculations. *At. Data Nucl. Data Tables* **96,** 271–298 (2010).

Wildfire Risk Map Based on DBSCAN Clustering and Cluster Density Evaluation

Muchamad Taufiq Anwar, Wiwien Hadikurniawati, Edy Winarno, Aji Supriyanto

Faculty of Information Technology, Universitas Stikubank Semarang, Jl. Tri Lomba Juang No 1 Semarang 50241, Central Java, Indonesia

taufiq@edu.unisbank.ac.id

Abstract. Wildfire risk analysis can be based on historical data of fire hotspot occurrence. Traditional wildfire risk analyses often rely on the use of administrative or grid polygons which has their own limitations. This research aims to develop a wildfire risk map by implementing DBSCAN clustering method to identify areas with wildfire risk based on historical data of wildfire hotspot occurrence points. The risk ranks for each area/cluster were then ranked/calculated based on the cluster density. The result showed that this method is capable of detecting major clusters/areas with their respective wildfire risk and that the majority of consequent fire occurrences were repeated inside the identified clusters/areas.

Keywords: wildfire risk map; clustering; DBSCAN; cluster density;

1. Introduction

Wildfire is one of the most notable disasters occurred around the world. Wildfires had caused a large amount of economic losses and environmental damaged. Preventive actions/managements are required in order to minimize the negative effect caused by wildfire. One of the main tasks in managing wildfire is the detection of the areas which have high wildfire risk. The determination of area with a high risk of wildfire or any geographical phenomena (*i.e.,* the spatial 'hotspot') often relied on the use of administrative or grid polygons which has their own limitations, as mentioned by Han and Shu [1]. Therefore, the detection/determination of high fire risk areas should implement 'unsupervised' methods that are independent of administrative or grid polygons. One of the available options is by implementing a clustering algorithm to detect clusters of points and to set boundaries for each cluster. This research aims to develop a wildfire risk map by implementing DBSCAN clustering method to identify areas with wildfire risk based on historical data of wildfire hotspot occurrence points. Risk ranks for each identified area/cluster were then ranked/calculated based on their density (number of hotspot points per km square). The resulted wildfire risk map is useful in wildfire management so that preventive/mitigating action can be done to minimize losses or other negative effects.

2. Methods

2.1. Wildfire Risk Assessment

Research often used historical data of wildfire to determine wildfire risk in certain areas. Recent research had explored the risk of fire spreading to the urban area in Australia [2]. Other research used

generalized additive model to estimate wildfire risk in Mediterranean area [3], and used artificial neural networks to predict wildfire risk in South Africa [4]. The historical data can be obtained from satellite images such as from NASA [5]. The risk model might be based on several variables related to wildfire, such as the meteorological variables [6-8], vegetation indices [6,9], and other variables [6,7,9]; or based only on historical wildfire data [10]. When relying only on historical wildfire data, assessments can be based on the number of or the location of wildfire hotspot occurrences. A recent reseach also had explored a rule-based approach to wildfire model based on historical wildfire data[11].

The identification of area with high fire occurrence/risk (the spatial 'hotspot') can also be done using spatial analysis such as the Anselin's Moran's I or LISA [12] and Getis-Ord Gi [13]. This approach is sensible since most geographical phenomena often show a spatial pattern (i.e. clustered) [14], including wildfire itself [15,16]. Even the evidence of spatial autocorrelation itself can be included in the model to make it better [17]. However, these analyses often use administrative polygons or grid polygons and require a high number of polygons to be used in a study area in order for the analysis to give a good result. Furthermore, the use of polygons itself also has its own drawbacks, namely the scale mismatch, shape mismatch, and location mismatch as mentioned in [1].

2.2. DBSCAN Clustering

Density-Based Clustering of Applications with Noise (DBSCAN) is a modern clustering algorithm which has the capability to detect cluster in spatial points data (coordinates) and not relying on polygons. DBSCAN was first introduced by Ester, et.al in 1996 [18]. DBSCAN has two parameters namely eps which represent maximum distance/radius from a point where the membership of other points enclosed within it is evaluated; and minpts which tell the minimum number of points to be considered as a member of a cluster within the radius of eps. DBSCAN works by giving each point a circle with the radius of determined eps, followed by the membership evaluation for each point enclosed in that circle. A point would fall into one of three categories, namely a core point, border point, or noise points. A point is assigned as core points if it has at least a number of member (enclosed) point equal to minpts within radius eps. A point is assigned as border points when a point is within eps but has a number of member points of less than minpts. Finally, if the point doesn't belong to the core or border points, it is assigned as noise points. Noise points are not a member of any clusters. A cluster is then defined as a set membership containing a combination of core points surrounded by border points. The pseudocode for the DBSCAN algorithm is presented in Algorithm 1 [19].

Algorithm 1: *DBSCAN Clustering*

```
DBSCAN(D, eps, MinPts)
    C = 0
    For each unvisited point P in dataset D
        mark P as visited
        N = getNeighbors (P, eps)
        If sizeof(N) < MinPts then
            mark P as NOISE
        Else
            C = next cluster
            expandCluster(P, N, C, eps, MinPts)
        End If
    End For

expandCluster(P, N, C, eps, MinPts)
        add P to cluster C
    For each point P' in N
        If P' is not visited
            mark P' as visited
                N' = getNeighbors(P', eps)
            If sizeof(N') >= MinPts
                N = N joined with N'
```

```
22:         End If
23:     End If
24:         If P' is not yet member of any cluster
25:         add P' to cluster C
26:         End If
27:     End For
```

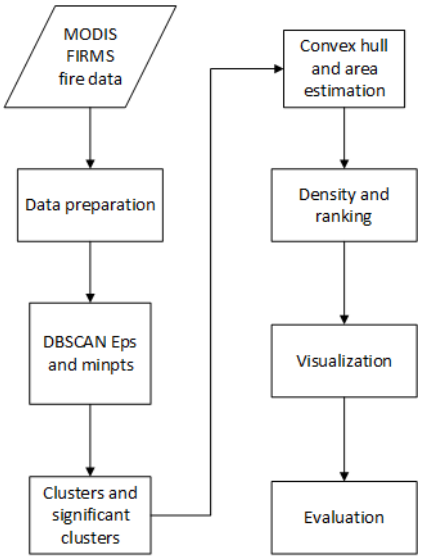

Figure 1. Research framework.

The research framework for this paper is shown in Figure 1. For the purpose of this research, DBSCAN is used since it has advantages over other clustering algorithms such as the K-Means clustering and Scan statistics. First, unlike the K-Means, DBSCAN does not require us to set a determined number of cluster k. This determination of k, of course, is not suitable for this research, since the number of identified clusters is merely a result of density evaluation of points in the data, *i.e.,* an "unsupervised" algorithm. Furthermore, DBSCAN can detect clusters with arbitrary shapes, while K-Means and Scan statistics only evaluate and produce clusters of circular shape. This circular shape, of course, is not suitable to be implemented on geographical data since geographical phenomena come in many shapes. Recent use of DBSCAN in geographical clustering includes retail agglomerations [20], and location recommendation in location-based social networks [21]. Recent research also applied the DBSCAN to detect clusters in raster images [22]. Despite years of proposed improvements, the original DBSCAN could still perform well as long as we pick a reasonable parameter [23].

In order to calculate the density of a cluster, we need to estimate the area of each cluster, which first we need to determine the boundary of the clusters. One of the available options is the convex hull algorithm. In mathematics, a convex hull is the smallest set (area) which allows any two points in that set to be connected without leaving the set. It is well understood using the analogy of a stretched rubber band which encloses a set of points (*i.e*., a cluster) [24]. Wildfire data were collected from the Moderate Resolution Imaging Spectroradiometer (MODIS) provided by the Fire Information for Resource Management System (FIRMS). This data is a result of automatic detection by NASA MODIS satellite for the anomaly of temperature/fire presence. For the purpose of this research, only data with 100 confidence were used. The data of the national wildfire archive were then filtered/clipped only for the study area.

DBSCAN clustering algorithm was done in R using 'dbscan' function in the 'dbscan' package. The determination of eps was first based on visual examination of 'knee' in the K-NN distance plot provided by 'kNNdistplot' function, provided in the same package. The experimentations of eps and minpts were done in multiple datasets to test their performance. The datasets were varied in the time and spatial scope. The best and final eps and minpts value to be used in this research were then picked based on the experimentation result. The DBSCAN algorithm resulted in points membership assigned as a member of a cluster or as a noise. Noise points were removed before the creation of convex hull polygons. Each polygon has the attribute of its area (in degree square). This attribute is automatically generated by the Convex Hull function in QGIS. These areas in degree square were then converted into the areas in kilometer square (at the equator, one degree of longitude/latitude is about 110.57 km). Our study area is located at the equator, spanning from latitude 02° 25' N to 01° 15' S. Clusters density were then calculated by dividing the number of points in each area/cluster by the cluster's area (in km square).

The risk ranks for each area/cluster were then ranked/calculated based on the density of the clusters. The rank is relative, where clusters with a density higher than the mean density are classified as a high

fire risk area, while clusters with a density lower than the mean density are classified as a medium fire risk area. The low fire risk area then is the area outside the identified clusters. The resulted clusters with their corresponding fire risk ranks were then visualized using QGIS. The resulted clusters were tested using the test dataset from the past two years. The tools used in this research are RStudio and QGIS 2.18.

3. Results and Discussion

The study area for this researh is Riau Province in Sumatra Island, Indonesia. Wildfire data from 2001 data 2017 were filtered only those with 100 confidence and were split into two datasets, 21252 training dataset has which ranged from 2001 to 2015, and 326 test dataset which ranged from 2016 to 2017. The wildfire locations of training dataset is shown in Figure 2a. The training dataset was run in the DBSCAN algorithm with eps of 0.02 degrees (~2.21 km) and minpts = 5. These values were based on experimentation which gave good clustering results. The DBSCAN algorithm in R package 'dbscan' resulted in 211 clusters with a total membership of 16142 points (76% of fire case data). Minor clusters that have historical fire counts less than 120 were then excluded. The 120 limits were estimated by the judgment of one fire case in 8 fire-months for 15 years. Convex hull polygons were created using QGIS function which also calculated the area of each cluster. The areas of each cluster (in kilometer square) were then calculated by multiplying the area (in degree square) with 110.57 km square (1 degree in equator ~ 110.57 km). Fire density for each cluster was then calculated by dividing the number of fire points in a cluster with the area (in kilometer square) of the corresponding cluster. The previous minor clusters exclusion had also eliminated low-density cluster with a density lower than 0,5 (which translated into less than one fire in an area of 2 km square). The result is 22 "significant" / major clusters which have high historical fire count and usually have a large area. These clusters were then assigned fire risk rank/label based on their density. The risk ranks were assigned based on their density compared to their mean. A density lower than the mean would be assigned as an area of medium fire risk, while a density higher than the mean is assigned as an area of high fire risk. The low fire risk areas are the areas which are not included in the final (major) clusters. This resulted in l4 medium fire risk clusters and 8 high fire risk clusters. One of the clusters in the high fire risk category has very high density and deemed as an outlier from other clusters. This cluster was then assigned as a very high fire density. The resulted clusters and their respective fire ranks are shown in Figure 2b. The area with a very high fire risk is located at the near top right of the study area.

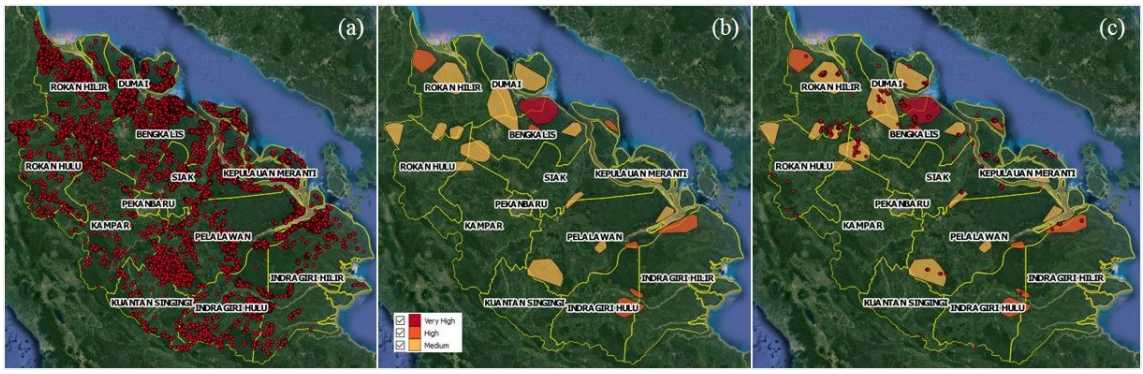

Figure 2. (a) Locations of fire hotspot within the study area from 2001 to 2015. (b) Resulted clusters with their color-coded risk ranks. (c) Recent wildfire cases overlayed with the resulted clusters.

The resulted clusters were then tested against fire data from the last two years (2016-2017) which have 326 fire points as shown in Figure 2c. Layer overlay and intersection we used to calculate the number of points within the resulted clusters and resulted in 229 of 326 or 70% fire point fall within final significant clusters. The detailed information for each cluster is shown in Table 1. The resulted clusters might reveal similarity in wildfire variables such as meteorological factors, vegetation, or land

type (peat or non-peat). From the spatial hotspot analysis view, each cluster resulted from the DBSCAN algorithm may also represent a hotspot (High-High) surrounded by 'warm' spots (High-Low). The hotspots are analogous to the core points, while the warm spots are analogous to border points.

Table 1. The resulted clusters and their attributes.

Cluster ID	Number of points (Training dataset)	Area (km square)	Density (Points per km square)	Risk Rank	Number of points (Test dataset)
1	4846	1043,89	4,64	Very High	45
2	1536	533,96	2,88	High	1
3	206	97,33	2,12	High	1
4	1249	603,16	2,07	High	10
5	194	110,46	1,76	High	15
6	839	513,08	1,64	High	0
7	162	109,70	1,48	High	0
8	164	111,10	1,48	High	10
9	371	262,43	1,41	Medium	4
10	279	200,49	1,39	Medium	0
11	214	169,80	1,26	Medium	4
12	366	301,52	1,21	Medium	0
13	1683	1388,49	1,21	Medium	24
14	834	691,11	1,21	Medium	19
15	173	152,54	1,13	Medium	0
16	256	270,24	0,95	Medium	0
17	168	219,24	0,77	Medium	37
18	583	761,50	0,77	Medium	15
19	689	966,70	0,71	Medium	26
20	164	243,95	0,67	Medium	11
21	244	369,38	0,66	Medium	0
22	475	930,61	0,51	Medium	6
	15695				**228**

4. Conclusion and Future Research

Wildfire risk assessment can be based on historical data of fire hotspot occurrence. This research built a model for fire-risk prone areas using DBSCAN clustering applied on historical wildfire data from 2001 to 2015 and followed by density evaluation to determine risk rank. The resulted clusters were then tested against recent wildfire data from the last two years, and it showed that 70% of the recent wildfire occurrence falls within the resulted cluster, which indicates good performance. The identified cluster calls the authorities to perform wildfire ignition prevention and other mitigation actions [25].

However, the convex hull algorithm used in this research has its own limitation in estimating area since it cannot create proper cluster boundary in complex cluster shapes. In that case, other cluster boundary estimation such as concave hull or buffer distance might work better, but some parameter tuning might be needed. Area estimation (in kilometer) also need to be reconsidered in a study area far

from the equator. Future research might also try to explore other or richer risk-ranking method. The determination of eps and minpts in DBSCAN, and also the risk ranking method could also be based on experts' judgment or against a certain standard from the authority.

References

[1] Han, H., & Shu, X. (2017). A Self-Adjusting Approach to Identify Hotspots. International Review for Spatial Planning and Sustainable Development, 5(2), 104-112.
[2] Price, O., Borah, R., Bradstock, R., & Penman, T. (2015). An empirical wildfire risk analysis: the probability of a fire spreading to the urban interface in Sydney, Australia. International Journal of Wildland Fire, 24(5), 597-606.
[3] Ager, A. A., Preisler, H. K., Arca, B., Spano, D., & Salis, M. (2014). Wildfire risk estimation in the Mediterranean area. Environmetrics, 25(6), 384-396.
[4] Lall, S., & Mathibela, B. (2016, December). The application of artificial neural networks for wildfire risk prediction. In 2016 International Conference on Robotics and Automation for Humanitarian Applications (RAHA) (pp. 1-6). IEEE.
[5] Farahmand, A., Reager, J. T., Behrangi, A., Stavros, E. N., & Randerson, J. T. (2017, December). Using NASA Satellite Observations to Map Wildfire Risk in the United States for Allocation of Fire Management Resources. In AGU Fall Meeting Abstracts.
[6] Nami, M. H., Jaafari, A., Fallah, M., & Nabiuni, S. (2018). Spatial prediction of wildfire probability in the Hyrcanian ecoregion using evidential belief function model and GIS. International journal of environmental science and technology, 15(2), 373-384.
[7] Guo, F., Su, Z., Wang, G., Sun, L., Lin, F., & Liu, A. (2016). Wildfire ignition in the forests of southeast China: Identifying drivers and spatial distribution to predict wildfire likelihood. Applied Geography, 66, 12-21.
[8] Mitri, G., Jazi, M., & McWethy, D. (2015). Assessment of wildfire risk in Lebanon using geographic object-based image analysis. Photogrammetric Engineering & Remote Sensing, 81(6), 499-506.
[9] Amalina, P., Prasetyo, L. B., & Rushayati, S. B. (2016). Forest Fire Vulnerability Mapping in Way Kambas National Park. Procedia Environmental Sciences, 33, 239-252.
[10] Nisa, K. K., Andrianto, H. A., & Mardhiyyah, R. (2014, October). Hotspot clustering using DBSCAN algorithm and shiny web framework. In 2014 International Conference on Advanced Computer Science and Information System (pp. 129-132). IEEE.
[11] M. T. Anwar, H. D. Pumomo, S. Y. J. Prasetyo, and K. D. Hartomo, "Decision Tree Learning Approach To Wildfire Modeling on Peat and Non-Peat Land in Riau Province," in *2018 International Conference on Advanced Computer Science and Information Systems (ICACSIS)*, 2018, pp. 409–415.
[12] Anselin, L. (1995). Local indicators of spatial association—LISA. Geographical analysis, 27(2), 93-115.
[13] Getis, A., & ORD, J. (1992). The analysis of spatial association by use of distance statistics Geographical Analysis 24 (3): 189–206.
[14] Griffith, D., & Chun, Y. (2016). Spatial autocorrelation and uncertainty associated with remotely-sensed data. Remote Sensing, 8(7), 535.
[15] Chou, Y. H., Minnich, R. A., Salazar, L. A., Power, J. D., & Dezzani, R. J. (1990). Spatial autocorrelation of wildfire distribution in the Idyllwild quadrangle, San Jacinto Mountain, California. Photogrammetric Engineering and Remote Sensing, 56(11), 1507-1513.
[16] Koutsias, N., Allgöwer, B., & Conedera, M. (2002, November). What is common in wildland fire occurrence in Greece and Switzerland?–Statistics to study fire occurrence pattern. In Proceedings of the 4th International Conference on Forest Fire Research (pp. 18-23).
[17] Portier, J., Gauthier, S., Robitaille, A., & Bergeron, Y. (2018). Accounting for spatial autocorrelation improves the estimation of climate, physical environment and vegetation's effects on boreal forest's burn rates. Landscape ecology, 33(1), 19-34.
[18] Ester, M., Kriegel, H. P., Sander, J., & Xu, X. (1996, August). A density-based algorithm for

discovering clusters in large spatial databases with noise. In Kdd (Vol. 96, No. 34, pp. 226-231).
[19] Vijayalaksmi, S., & Punithavalli, M. (2012). A fast approach to clustering datasets using dbscan and pruning algorithms. International Journal of Computer Applications, 60(14).
[20] Pavlis, M., Dolega, L., & Singleton, A. (2018). A Modified DBSCAN Clustering Method to Estimate Retail Center Extent. Geographical Analysis, 50(2), 141-161.
[21] Yuan, Z., & Li, H. (2016, June). Location recommendation algorithm based on temporal and geographical similarity in location-based social networks. In 2016 12th World Congress on Intelligent Control and Automation (WCICA) (pp. 1697-1702). IEEE.
[22] Trifonov, G. M., Zhizhin, M. N., Melnikov, D. V., & Poyda, A. A. (2017). VIIRS Nightfire Remote Sensing Volcanoes. Procedia computer science, 119, 307-314.
[23] Schubert, E., Sander, J., Ester, M., Kriegel, H. P., & Xu, X. (2017). DBSCAN revisited, revisited: why and how you should (still) use DBSCAN. ACM Transactions on Database Systems (TODS), 42(3), 19.
[24] Berg, M. D., Cheong, O., Kreveld, M. V., & Overmars, M. (2008). Computational geometry: algorithms and applications. Springer-Verlag TELOS.
[25] Calkin, D. E., Cohen, J. D., Finney, M. A., & Thompson, M. P. (2014). How risk management can prevent future wildfire disasters in the wildland-urban interface. Proceedings of the National Academy of Sciences, 111(2), 746-751.

Analysis of Water Quality and River Waters Microbology for Manifestation of Food Safety

Rizky Muliani Dwi Ujianti and Althesa Androva
Faculty of Engineering and Informatics, Universitas PGRI Semarang, Jl. Sidodadi Timur 24. Dr. Cipto Semarang, Indonesia

rizkymuliani@upgris.ac.id

Abstract. Banjir Kanal Barat is a river in the Garang watershed, Semarang City, Central Java, Indonesia. Its function is as a source of water for the community. The level of pollution in this river is already high. The purpose of this study is to provide advice to governments, communities and related stakeholders to realize integrated river management, and fisheries-based food security is achieved. This research method is: analyzing the water quality of the Banjir Kanal Barat river, and analyzing the amount of faecal and total coliform bacteria content in the Banjir Kanal Barat river, and analyzing how to overcome the decline in the quality of waters of the Banjir Kanal Barat river due to faecal and total coliform bacteria pollution. The results showed that the water quality at the research location was still in the quality standard. The content of coliform dan faecal bacteria at the study site exceeds the quality standard, this is due to the influence of domestic waste from households. The thing that needs to be done is counseling the existence of a clean and healthy life, especially for people who are still throwing domestic waste into the river. The existence of water purification equipment is also very necessary to overcome this problem. Water quality management can be done with policy analysis. Regulations related to water quality management can be analyzed and then given solutions and recommendations related to these rules so that policies can be taken that are sustainable, integrated, and coordinated between various parties in managing river water quality and food security.

Keywords: food security, water quality, river, faecal coliform, total coliform

1. Introduction

Semarang is the capital city of the province of Central Java. Industries in the city of Semarang are food, beverages, pharmaceuticals, textiles and so on, industries that do not properly process waste will pollute the river to the estuary region. Besides, the problem that occurs in the Banjir Kanal Barat (BKB)/Kanal Banjir Barat (KBB) river is the high coliform bacteria. The high faecal coliform comes from upstream areas polluted by domestic waste from housing, animal husbandry activities and leachate from manure [1]. River management must be synergistic between physical, chemical and biological aspects. This research is a study that elaborates on these aspects: water temperature, water pH, Dissolved Oxygen (DO), and microbiological aspects of river water environment: Total Coliform and Faecal Coliform and increased food safety in the fisheries. Fisheries production in Indonesia is 5.6 million tons/year in 2018. Industrial waste, especially fisheries, if not managed properly will have a negative impact on river waters causing eutrophication [2]. Management of the fisheries sector is faced with various problems namely ownership (common property resources) and the biological, chemical and physical complexity of the waters. These three aspects, if not managed properly, will lead to water pollution, which will affect the health of fish and decrease the quality of fishery products [3] which will have an impact on food security.

2. Methods

Sampling station area in Banjir Kanal Barat River, Garang watershed, Semarang, Central Java, Indonesia (Figure 1). Banjir Kanal Barat river is an estuary in the Laut Jawa. Water quality parameters studied were temperature, pH and DO. DO, temperature and pH were measured using a DO meter type

Lutron 5510. The microbiological parameters studied were faecal coliform and total coliform. Total coliform was analyzed by APHA test method 22nd, 9921.F: 2012. Faecal coliform was analyzed by the APHA 22nd, 9921.D: 2012 test method.

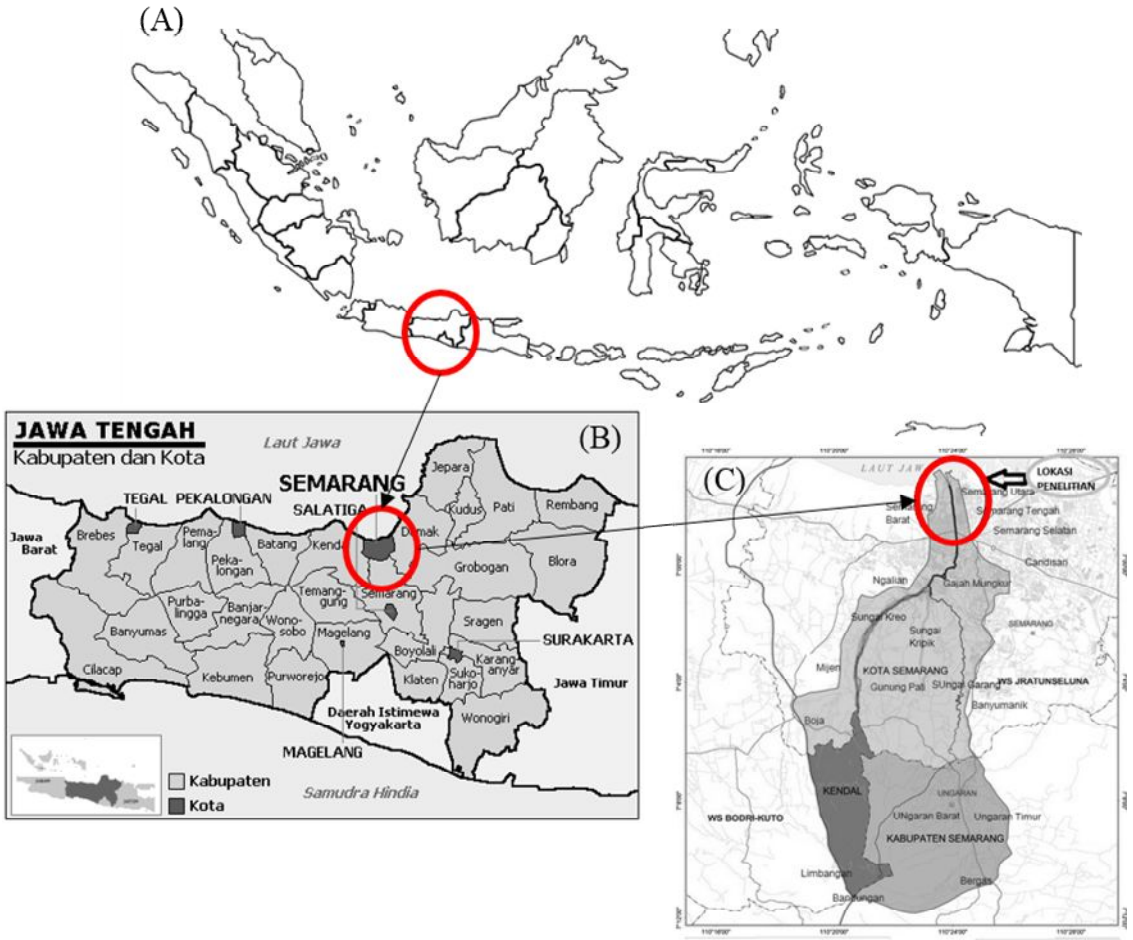

Figure 1. Study area: the map of the Indonesia (A), Central Java Province (B), Location of Banjir Kanal Barat River, Semarang, Central Java Province, Indonesia (C)

3. Results and Discussion

3.1. Water Quality

Dissolved Oxygen (DO) concentration is influenced by the chemical, physical and microbiological aspects of water. The content of coliform bacteria is high, causing low dissolved oxygen concentrations [4]. A decrease in DO is one indicator of decreased water quality [3]. This area is an area of aquaculture that is estimated to have a lot of ammonia waste from fish feed. This can cause a bad influence on the aquatic environment [27]. A good DO concentration for fisheries is 3 mg/L [5]. The range of DO at the study site is 4.6-6.5 mg/L. DO quality standard according to PP No. 82 of 2001 (Indonesia Regulation) class III that is equal to 12.2 mg / L. The DO content at the six sampling points in this study is still in the class III quality standard. At the 1C sampling point the DO conditions were the lowest compared with another sampling point, this is presumably due to the largest input of waste at this sampling point, the DO content in low waters can increase fish respiration through gills, so that the flow of water containing toxic will increase [6]. DO content is influenced by photosynthesis of water, diffusion from the air, water temperature, the process of respiration by aquatic animals that occur at the bottom of the water [7]. Conditions of water discharge are quite heavy and extreme river slope due to the inclined plane at this location three caused water bubbles to cause DO conditions to be high [8]. Changes in DO content can be daily, seasonal, and depend on mixing, water mass movement, respiration, photosynthetic activity and waste entering the water body [9]. DO requirements for fish are divided into two aspects: the consumptive needs of fish that depend on their metabolism and the

aquatic environmental requirements of certain species [10]. The DO content graph is presented in Figure 2.

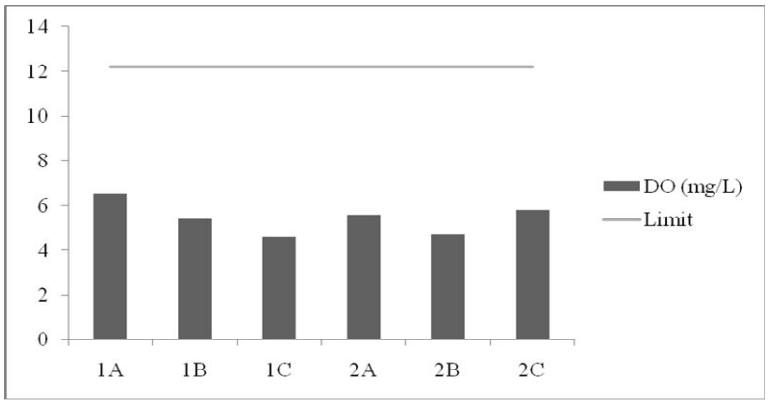

Figure 2. Concentration of DO (mg/L) in Sampling Station

pH is very important in wastewater treatment because it affects the life of the organism. The pH value at the location of this study is between 8.01 - 8.06. The value of natural pH and water that is not polluted is pH 7. The pH quality standards listed in PP 82/2001 classes I, II, and III are 6-9 while class IV is between 5-9. Class I, II, and III standards are suitable for the life of almost all aquatic organisms. Water pH at all sampling points still in PP No 82 of 2001 quality standards. The pH content is influenced by waste disposal which converts the concentration of hydrogen ions in water to acid or base because of its chemical content contained [11]. The reduced pH is influenced by an increase in rainfall intensity due to the entry of organic material into the body of water carried by the rain that enters the river [11]. The decrease in pH and salinity of waters can cause heavy metal toxicity. High hardness can reduce the toxicity of heavy metals. Heavy metals in water with high hardness to form complex compounds that settle in water [12]. An increase in pH in the waters will reduce the solubility of metals in water because an increase in pH changes the stability of the form of carbonate into hydroxide which forms bonds with particles in water bodies so that it will settle to form mud. pH affects the toxicity of a chemical compound [13]. Water pH affects plants and aquatic animals, so it is often used to determine the condition of good or poor water quality as a habitat for aquatic biota [11]. The pH is presented in Figure 3.

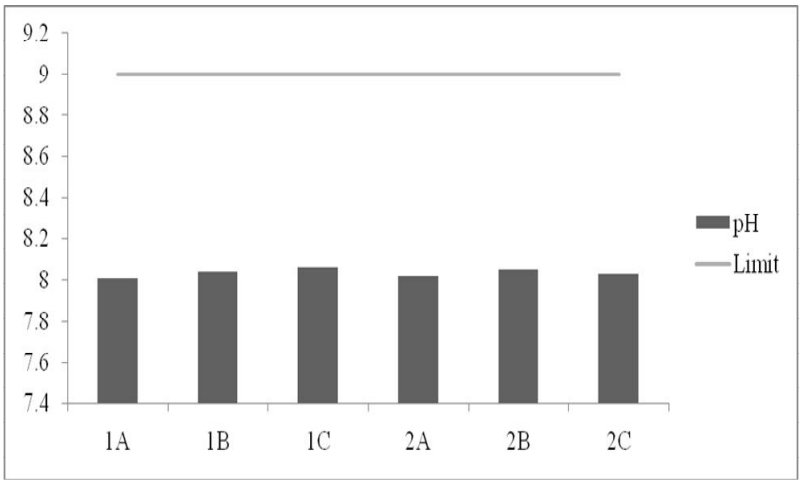

Figure 3. pH (mg/L) in Sampling Station

The temperature at the study site between 29.60C - 30.90C. Low temperatures occur due to measurements in the morning, so that not much intensity of sunlight to the river [14]. Normal water temperature in the river area is 27°C-30°C [3]. Temperature and pH are indicators for certain bacteria, for example, coliform bacteria that are tolerant of the mesophyll temperature range (25-37oC), and

neutrophil pH (6.7 - 7.5) [11]. Water temperature is always related to average air temperature, which varies with the seasons [3]. Increased temperature in the river can cause heavy metal toxicity to increase [12]. The temperature in waters can be influenced by solar radiation, solar position, geographical location, season, cloud conditions and the process of interaction between water and air, such as heat transfer, evaporation and wind [15]. The correlation between air temperature and water temperature at daily, weekly, or monthly times is generally used in modeling linear or nonlinear regression types developed to predict changes in flow temperature from air temperature [16]. The temperature is presented in Figure 4.

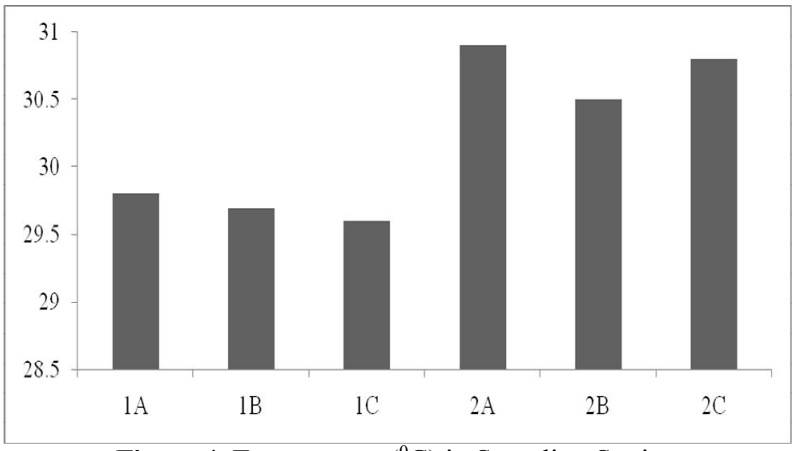

Figure 4. Temperature (^{0}C) in Sampling Station

3.2. Microbiology

River flow, urbanization, industrialization, land use, and rainfall are factors that influence the content of Fecal coliform bacteria. Build public toilets on the river causes the river to be polluted by human waste which is a source of disease. The presence of bacteria in rivers is an indicator of declining water quality. Bacteria in human waste include *Escherichia coli, Shigella sp., Vibrio cholerae, Campylobacter jejuni* and *Salmonella,* these bacteria are members of fecal coliform, which causes diarrheal disease. One way to measure total coliform, faecal coliform, or specific organisms such as *C. perfringens* or *E. coli* is that many animals have faecal indicator bacteria (FIB) in their feces [17]. Communities around watersheds that make rivers as their public toilets make river waters polluted by bacteria [9]. The distance of the septic tank to the water source and recommended is 10 meters [18]. The content of Faecal Coliform in the study location ranged from 11,000 to 79,000 MPN /100 mL. The quality standard for total coliform in PP No. 82 of 2001 amounted to 2000 ml /100 mL. The total coliform content in this study site exceeds the quality standard. Faecal coliform is used as an indicator of water pollution originating from household waste. A faecal coliform concentration>2000 MPN/100 mL is considered harmful to human health [19]. The concentration of coliform in the downstream location depends on the concentration of coliform in the upstream, and land use. Fecal coliforms become the standard needed to monitor and report microbial contamination [20]. Settlements that do not have drainage can affect coliform bacteria. Settlements that do not have a sewage treatment system, human waste is discharged directly and can affect the high fecal coliform [21]. The presence of large coli bacteria influences human life, as evidenced by the quality of drinking water, bacteriologically the level is determined by the presence of these bacteria [22]. Faecal coliform is presented in Figure 5.

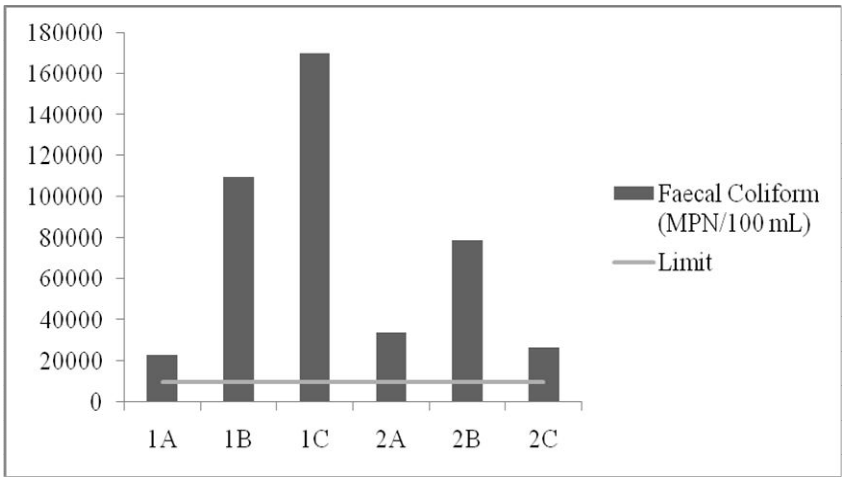

Figure 5. Faecal Coliform (MPN/100mL) in Sampling Station

A total coliform is a group of bacteria that is used as an indicator of pollution [23]. Total Coliform content in the study area ranged from 33,000 to 79,000 MPN/100 ml. Quality standard for total coliform in PP No. 82 of 2001 amounting to 10,000 MPN/100 ml. The total coliform content in this study site exceeds the quality standard. This is due to the presence of excess domestic waste in the study site because there are still many people (especially the homeless), who live around the river and immediately defecate in the river. Each person emits 100-400 billion coliforms per day in addition to other types of bacteria. The presence of *E. Coli* in water indicates fecal contamination and causes the possibility of pathogenic diseases such as bacteria, viruses and parasites and so on. The presence of coliform bacteria is caused by human activity and causes various diseases in digestion [24]. Total coliform density increases rapidly in summer at high temperatures [25]. Physical and chemical properties of waters can affect the survival rate, decay or growth of coliform bacteria. Suspended solids can affect coliform survival or growth by adsorbing coliforms and protecting it from harmful factors, such as UV radiation, metals, and bacteriophage attacks. Suspended solids can also provide coliform bacteria, organic and inorganic nutrients in particles. Coliform mortality rates increase with high water temperatures, whereas temperatures are positively correlated with coliforms. Too high pH is dangerous for the survival of coliforms [26]. The presence of bacteria in the water is influenced by abiotic factors such as temperature, pH, oxygen, humidity, and biotic factors. Water to be used for drinking, domestic, agricultural and industrial purposes is very important to be tested first on the physical, chemical and microbiological parameters of water [11]. Total coliform is presented in Figure 6.

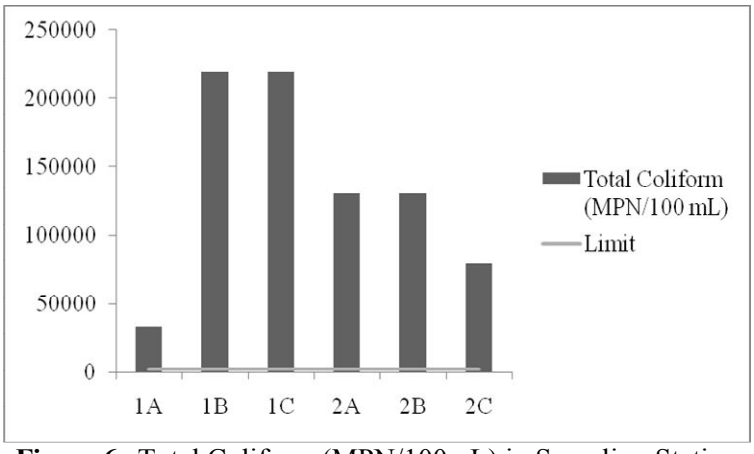

Figure 6. Total Coliform (MPN/100mL) in Sampling Station

4. Conclusion and Recommendation

Water quality at the study site still meets quality standards. The high coliform bacteria at the study site were caused by domestic and industrial waste discharges that did not meet the criteria for good waste disposal. Policy analysis needs to be done by the government to see the effectiveness of some rules regarding water quality. This research needs to be continued continuously, to monitor river water quality sustainably, and to analyze the most appropriate methods to be used in reducing some water quality parameters that exceed the quality standards.

Acknowledgements

Authors would like to thank to LPPM Universitas PGRI Semarang who gave the research fund, with Contract Number: 267.E/EST/LPPM_UPGRIS/III/2019

References

[1] Marlena, B. (2012, September). Kajian Pengelolaan Sub DAS Garang Hulu terhadap Kualitas Air Sungai. In Seminar Nasional Pengelolaan Sumberdaya Alam dan Lingkungan.

[2] Ibrahim, B., & Suptijah, P. (2009). The Utilization of Chitosan on Fishery Industrial Wastewater Treatment. Jurnal Pengolahan Hasil Perikanan Indonesia, 12(2).

[3] Syofyan, I., & Nasution, P. (2012). Studi Kualitas Air Untuk Kesehatan Ikan Dalam Budidaya Perikanan Pada Aliran Sungai Kampar Kiri. Jurnal Perikanan Dan kelautan, 16(01).

[4] Brontowiyono, W., Kasam, K., Ribut, L., & Ike, A. (2013). Strategi Penurunan Pencemaran Limbah Domestik di Sungai Code DIY. Jurnal Sains dan Teknologi Lingkungan, 5(1), 36-47.

[5] Kurniasih, N. (2002). Pengelolaan DAS Citarum berkelanjutan. Jurnal Teknologi Lingkungan, 3(2), 82-91.

[6] Hidayah, A. M., Purwanto, P., & Soeprobowati, T. R. (2014). Biokonsentrasi faktor logam berat Pb, Cd, Cr dan Cu pada ikan nila (*Oreochromis niloticus Linn*.) di karamba Danau Rawa Pening. Bioma: Berkala Ilmiah Biologi, 16(1), 1-9.

[7] Ratnapuri, V. V., Zainuri, M., Widowati, I., & Supriyanto, J. (2013). Kesuburan Perairan Berdasarkan Struktur Komunitas Fitoplankton Dalam Memprediksi Daerah Penangkapan Kerang Simping (*Amusium Pleuronectes*) Di Perairan Pemalang.

[8] Prabowo, R., & Subantoro, R. (2012). Kualitas Air dan Beban Pencemaran Pestisida di Sungai Babon Kota Semarang. Mediagro, 8(1).

[9] Warman, I. (2017). Uji kualitas air muara sungai Lais untuk perikanan di Bengkulu Utara. Jurnal Agroqua: Media Informasi Agronomi dan Budidaya Perairan, 13(2), 24-33.

[10] Zonneveld, N., Huisman, E. A., & Boon, J. H. (1991). Prinsip-prinsip budidaya ikan. PT Gramedia Pustaka Utama.

[11] Rahmawati, R., Fitria, L., & Syafitri, L. (2017). Correlation of Physical-Chemical Parameters to Total Coliform Value in Jawi River, Pontianak, West Kalimantan. Biosaintifika: Journal of Biology & Biology Education, 9(2), 370-379.

[12] Kurniawati, S., Nurjazuli, N., & Raharjo, M. (2017). Risiko Kesehatan Lingkungan Pencemaran Logam Berat Kromium Heksavalen (Cr VI) pada Ikan Nila (*Oreochromis niloticus*) di Aliran Sungai Garang Kota Semarang. Higiene: Jurnal Kesehatan Lingkungan, 3(3), 152-160.

[13] Usman, S., La Nafie, N., & Ramang, M. (2013). Distribusi kuantitatif logam berat Pb dalam air, sedimen dan ikan merah (Lutjanus erythropterus) di sekitar perairan pelabuhan Parepare. Marina Chimica Acta, 14(2).

[14] Gitarama, A. M., Krisanti, M., & Agungpriyono, D. R. (2016). Komunitas Makrozoobentos dan Akumulasi Kromium di Sungai Cimanuk Lama, Jawa Barat. Jurnal Ilmu Pertanian Indonesia, 21(1), 48-55.

[15] Bakti, L. M. (2010). Study of tidal inundation potential at Semarang City and its solutions. Diponegoro University.

[16] Kędra, M., & Wiejaczka, L. (2018). Climatic and dam-induced impacts on river water temperature: Assessment and management implications. Science of the Total Environment, 626, 1474-1483.

[17] Aburto-medina, A., Shahsavari, E., Salzman, S. A., Kramer, A., Ball, A. S., & Allinson, G.

(2019). Elucidation of the microbial diversity in rivers in south-west Victoria, Australia impacted by rural agricultural contamination (dairy farming). Ecotoxicology and Environmental Safety, 172, 356–363.

[18] Puspitasari, D. E. (2009). Dampak pencemaran air terhadap kesehatan lingkungan dalam perspektif hukum lingkungan (Studi kasus sungai Code di Kelurahan Wirogunan Kecamatan Mergangsan dan Kelurahan Prawirodirjan Kecamatan Gondomanan Yogyakarta). Mimbar Hukum-Fakultas Hukum Universitas Gadjah Mada, 21(1), 23-34.

[19] Tampubolon, R., Sanim, B., Saeni, M., & Boer, R. (2012). Analysis of Environmental Quality Changes of Citarum Watershed of West Java and their Effects on Operational Costs of Hydroelectric Power Plans and the Regional Drinking Water Companies (Case Study at Saguling, Cirata, and Jatiluhur Hydroelectric Power Pl.

[20] BenDor, T. K., Jordanova, T. V., & Miles, B. (2017). A geospatial analysis of land use and stormwater management on fecal coliform contamination in North Carolina streams. Science of The Total Environment, 603, 709-727.

[21] Reder, K., Flörke, M., & Alcamo, J. (2015). Modeling historical fecal coliform loadings to large European rivers and resulting in-stream concentrations. Environmental Modelling & Software, 63, 251-263.

[22] Widiyanti, N. L. P., & Ristiati, N. P. (2004). Qualitative analysis of coliform bacteria at some shops refilled drinking water in Singaraja Bali. Jurnal Ekologi Kesehatan, 3(1), 64-73.

[23] Pakpahan, R. S., Picauly, I., & Mahayasa, I. N. W. (2015). Cemaran Mikroba Escherichia coli dan Total Bakteri Koliform pada Air Minum Isi Ulang. Kesmas: National Public Health Journal, 9(4), 300-307.

[24] Divya, A. H., & Solomon, P. A. (2016). Effects of some water quality parameters especially total coliform and fecal coliform in surface water of Chalakudy river. Procedia Technology, 24, 631-638.

[25] An, Y. J., Kampbell, D. H., & Breidenbach, G. P. (2002). Escherichia coli and total coliforms in water and sediments at lake marinas. Environmental Pollution, 120(3), 771-778.

[26] Hong, H., Qiu, J., & Liang, Y. (2010). Environmental factors influencing the distribution of total and fecal coliform bacteria in six water storage reservoirs in the Pearl River Delta Region, China. Journal of Environmental Sciences, 22(5), 663-668.

[27] Ujianti, R. M. D., Anggoro, S., Bambang, A. N., Purwanti, F. & Androva, A. (2019). Environmental Study on Phytoplankton in Garang Watershed, Central Java, Indonesia and Its Water Quality, IOP Conference Series: Earth and Environmental Science, 246, 012070.

Fractionation of metabolite compound from *Medinilla speciosa* and their antioxidant activities using ABTS$^{\cdot+}$ radical cation assay

Rissa Laila Vifta and Fania Putri Luhurningtyas

Department of Pharmacy, Faculty of Health Science, Universitas Ngudi Waluyo, Indonesia

rissalailavifta@gmail.com

Abstract. Phenolic compounds are one of the main parts in secondary metabolites. Parijoto fruit is a family of Melastomataceae which contains flavonoids as phenolic compounds which are known to have antioxidant potential. Flavonoids have an-OH groups that play an active role as free radical scavengers. The study was conducted as initial screening in testing the antioxidant activity of extracts and fractions of the Parijoto fruit (*Medinilla speciosa*). The study began with the phytochemical screening process using the Thin Layer Chromatography method to ensure the presence of flavonoid content in extracts and fractions of parijoto fruit, then proceed with the measurement of antioxidant power. Testing the antioxidant activity using the ABTS method (2,2 azinobis (3-ethylbenzothiazolin) -6-sulfonic acid) which is specific, simple and easy to apply. Parijoto fruit extracts and fractions were made in a series of concentrations, measured antioxidant activity, and each IC_{50} value was determined. Phytochemical screening test results showed the presence of flavonoids in extracts and fractions of parijoto fruit. The results of measurements of antioxidant power in extracts and fractions of parijoto fruit gave IC_{50} values of 6,520 ppm in ethanol extracts with very strong antioxidant categories. The n-hexane fraction produced an IC_{50} value of 118,424 ppm with a moderate antioxidant category, while the IC_{50} value of ethyl acetate and ethanol fractions was 4,246 ppm and 3,874 ppm, respectively, with a very strong antioxidant category. The activity and value of IC_{50} produced by extracts and fractions of Parijoto fruits showed potential as a candidate of antioxidant.

Keywords: ABTS, Antioxidant, Flavonoids, Medinilla speciosa, Phenolic

1. Introduction

Antioxidants are substances that play a role in preventing oxidation reactions. An antioxidant can contribute an electron to a free radical, so free radical formation can be inhibited [1]. Free radicals can have adverse effects such as aging, DNA damage, cancer, stroke, and other cardiovascular [2-3]. Free radicals can also reduce endogenous antioxidant activity in the body, thus requiring the presence of exogenous antioxidants [4].

Endogenous antioxidants are synthesized through metabolic processes and play a role in repairing body cell damage caused by free radicals, while exogenous antioxidants are antioxidants obtained from external sources such as food [5]. One of the exogenous antioxidants that play a role in the process of inhibiting free radicals comes from natural ingredients. Some uses of natural ingredients as exogenous antioxidants are due to economic factors, available in large quantities, as well as smaller side effects than synthetic antioxidants [6].

Medinilla speciosa or better known as Parijoto Fruit, contains metabolite compounds such as

flavonoids, saponins, tannins, and glycosides [7]. Parijoto fruit has traditionally been widely used by the public especially pregnant women in maintaining the health of the fetus. The content of phenolic compounds such as flavonoids in parijoto fruit has the potential as an antidote to free radicals. Phenolic compounds derived from natural substances have antioxidant activity by inhibiting free radicals and other reactive oxygen species [8].

Antioxidant activity testing can be done through the DPPH, ABTS, FRAP, ORAC, and FIC methods. Maesaroh et al., [9] compared the DPPH, FRAP, and FIC antioxidant test methods and obtained the result that the FIC method was less sensitive than the other two methods. Another study by Floegel et al., [10] states that the antioxidant activity of fruits, vegetables, and several other foodstuffs measured using the ABTS method results in higher significance values than measurements using the DPPH method. The pigments and hydrophilic content of the antioxidant compounds are more sentimental on the measurement using ABTS compared to DPPH.

ABTS (2.2 azinobis (3-ethylbenzothiazolin) -6-sulfonic acid) is one method of antioxidant testing that is easily applied, simple, and flexible in measuring the antioxidant activity that is hydrophilic or lipophilic in food extracts and liquids. Spirulina platensis produces higher antioxidant and anti-radical activity compared to DPPH [11]. The ABTS method can give an idea of the deterrence of free radicals by an antioxidant. The mechanism of ABTS begins with the formation of radicals between ABTS salts and potassium permanganate or potassium persulfate oxidants. BTS absorbance was measured at a specific wavelength of 734 nm [12].

This research will further examine the potential of Parijoto fruit as a natural antioxidant. Parijoto fruit extraction and fractionation were carried out using solvents with different levels of polarity. Testing the antioxidant activity using the ABTS method (2.2 azinobis (3-ethylbenzothiazolin) -6-sulfonic acid). Research is expected to provide an overview and further study regarding the use of natural materials in the field of phytopharmaca.

2. Materials and Methods

2.1. Materials

The main ingredient used is parijoto fruit powder derived from purplish parijoto fruit obtained from Colo Village, Kudus District. Test reagents include ABTS (2.2 azinobis (3-ethylbenzothiazolin)-6-sulfonic acid), $K_2S_2O_8$ from Sigma Aldrich, Methanol pro analysis from Merck, Aquadest, Ethanol 96% pro analysis Brataco, ethyl acetate, n-hexane, acid $K_2S_2O_8$ from Sigma Aldrich, Methanol pro analysis from Merck, Aquadest, Ethanol 96% pro analysis Brataco, ethyl acetate, n-hexane, acid glacial acetate, n-butanol from CV. Bratachem, and ammonia vapor.

Parijoto fruit powder is extracted by maceration method, then fractionated with three solvents (n-hexane, ethyl acetate, and ethanol). The active compound was identified by thin layer chromatography method. Parijoto fruit extracts and fractions were measured for their antioxidant activity by the ABTS method and IC_{50} values were determined.

2.2. Methods

2.2.1. Extraction and Fractionation

Parijoto fruit extraction was carried out by maceration method using two different solvents, namely 70% ethanol and 96%. The purpose of using solvent variations is to find out the best solvent that produces the most optimal yield. Extracts with optimal yield are then fractionated in stages using n-hexane, ethyl acetate, and ethanol solvents.

2.2.2. Flavonoid screening using TLC

Flavonoids were identified using thin layer chromatography with a modified procedure of Kumar et al., [13]. Silent silica phase GF254 and mobile phase used were n-butanol: glacial acetic acid: aquades. Flavonoid spotting viewers use ammonia vapor.

2.2.3. Antioxidant Activity Test with ABTS (Shalaby and Shanab, 2013)

Antioxidant measurement begins with determining the maximum wavelength of ABTS solution in the range of 600-800 nm and proceeds with determining the operational time or operating time. The antioxidant activity that continued by measuring each sample extract and fraction of the Parijoto fruit according to the flow diagram in Figure 1.

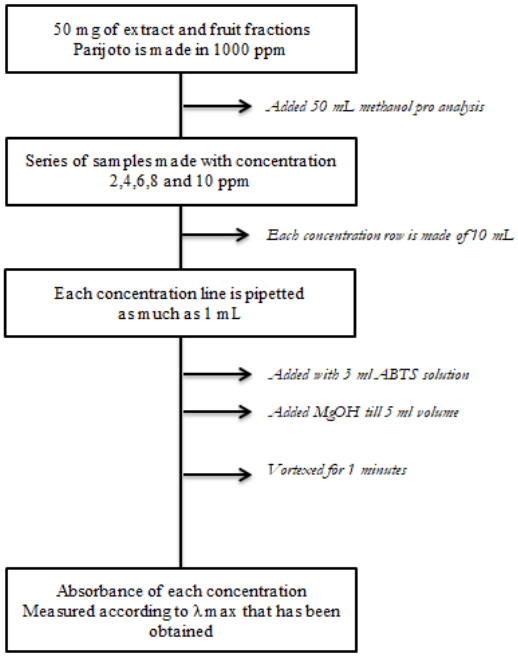

Figure 1. Mechanism of radical scavenger using $ABTS^{\cdot+}$ assay

3. Results and discussion

3.1. Extraction and Fractionation

Parijoto fruit extraction was carried out using ethanol solvents with different concentrations. Extraction with 70% ethanol solvent produced as much as 46 grams of thick extract from 300 grams of parijoto simplicia with a yield of 15.3%. Parijoto fruit extraction with 96% ethanol solvent resulted in a thick extract of 55.7 grams with a yield of 18.5% according to the results shown in Table 1. 96% ethanol solvent produced a greater yield than 70% ethanol solvent.

Table 1. Rendement of parijoto fruit exctract using etanol 70% and 96% solvent

Solvent	Weight of simplicia (gram)	Weight of exctract (gram)	Rendement (%)
70%	300	46,00	15,3
96%	300	55,70	18.5

The difference in yield in the two extraction processes is influenced by the difference in polarity between the two solvents and their interaction with the active compound contained in the fruit of Parijoto. The ideal solvent for finding simplicia fruit, leaves, fruit flesh is a mixture of alcohol-water with a concentration of 96% [14]. According to Senja et al., [15], ethanol 96% is capable of producing optimum yield and absorption in most fruit simplicia.

Fractionation of parijoto fruit is carried out in stages using three solvents with different polarity levels. Maceration extracted liquid-liquid fractionated with n-hexane, ethyl acetate and ethanol as a solvent. The use of different solvents allows the interest of active compounds in parijoto fruit and optimizes the process of withdrawal. The n-hexane fraction produced the greatest weight fraction compared to the ethyl acetate and ethanol fractions as shown in Table 2.

Table 2. Fractination result of parijoto fruit within n-hexane, ethyl acetate, and etanol solvent

Fraction	Weight of exctract (grams)	Weight of fraction (grams)
n-heksan	10,00	7,45
Etil asetat	10,00	2,01
Etanol	10,00	7,11

Luís et al., [16] and Gullón et al., [17] reported that fractionation allows the separation of active compounds according to their polarity with the principle of like dissolved like. Fractionation with n-hexane solvent is able to attract non-polar compounds in parijoto fruit, while ethyl acetate attracts semi-polar compounds. Fractionation with ethanol solvents is expected to increase the activity of polar active compounds in extracts of Parijoto Fruit (*Medinilla speciosa*), one of which is phenolic and flavonoid compounds which have antioxidant activity.

3.2. Flavonoids with TLC

Screening of the antioxidant activity of extracts and fractions of parijoto begins with the determination and identification of its active compounds. Determination shows that the test plants used are *Medinilla* species of the genus Melatomaceae. The identification results in Table 3 shown that both extracts and fractions of positive Parijoto fruit contain flavonoid compounds. Flavonoid compounds constitute most of the phenolic groups in natural materials which act as antidotes to free radicals.

Table 3. Identification of metabolite secondary compound of parijoto fruit using TLC

Sample	UV_{254} light	Rf	Amoniac vapor
Rutin	Brown spot	0.98	Yellowish green
Exctract	Brown spot	0.88	Yellowish green
FH	Brown spot	0.42	Yellowish green
FEA	Brown spot	0.91	Yellowish green
FE	Brown spot	0.98	Yellowish green

Keterangan :
FH : n-heksan fraction
FEA : ethyl acetate fraction
FE : ethanolic fraction

Thin layer chromatography (TLC) can be used effectively in the process of screening and evaluating the content of metabolites in a natural material. The chromatogram pattern produced at the time of separation with TLC provides a clear picture of the stability of natural materials. Other advantages of using TLC as a separation method include simple, applicable, and high speed separation method [18].

Flavonoid compounds in extracts and fractions of Parijoto fruit were identified by the mobile phase of n-butanol: glacial acetic acid: aquades (3: 1: 1) with high polarity properties. The choice of solvent is related to the nature of the compound and the stationary phase used. The solvent is not carcinogenic and does not react with the sample at the time of testing [13]. The stationary phase used is silica GF254 (Merck®) which has been widely used to separate phenolic compounds, alkaloids, fatty acids, sterols, and terpenoids.

Chromatographic results on extracts and fractions showed the presence of flavonoid compounds which were marked with brown spots when exposed to UV_{254} light and yellowish green spots with

ammonia vapor. The existence of flavonoids in natural materials, one of which is characterized by the presence of yellow fluorosis [19]. Flavonoids include phenolic compounds that have activity as exogenous antioxidants. Flavonoids are able to donate hydrogen atoms to free radicals, so that free radicals become unreactive.

3.3. Radical scavenger activity of parijoto fruit extract

Antioxidant activity begins with determining the maximum wavelength obtained in the 752 nm region. Determination of the maximum wavelength is done to measure the absorbance of compounds in the visible area, so that maximum absorption is obtained. The blank used in the test was methanol pro analysis. Antioxidant activity is determined by observing changes in color intensity in the ABTS solution used. The results of antioxidant activity tests on parijoto fruit extracts are shown in Table 4. Antioxidant activity is shown by an increase in the percentage of antioxidant activity as the extract concentration increases. IC_{50} value on parijoto fruit extract was 6,520 ppm with a very strong antioxidant category.

Table 4. Antioxidant activity of parijoto fruit exctract

Concentration (ppm)	Abs.	% Inhibition	IC_{50} (ppm)	Category
2	0.388	14.46		
4	0.301	33.77		
6	0.181	60.06	6.520	Very strong
8	0.166	63.51		
10	0.173	61.97		

The antioxidant activity of extracts and fractions of parijoto fruit was tested by the ABTS method (2.2 azinobis (3-ethylbenzothiazolin)-6-sulfonic acid). $ABTS^{\cdot+}$ is a radical source obtained from the activation process through the addition of potassium persulfate. Free radical reduction mechanism is characterized by a decrease in absorbance and a decrease in the color intensity of the test solution. The higher the antioxidant activity, the greater the intensity of lossing color produced during the testing process.

Antioxidant test on ethanol extract of parijoto fruit showed that the greater the concentration of the extract, the decreased intensity of absorbance was stronger as shown in Figure 2. The correlation between inhibitory activity (radical scavenger) with concentration, then used to determine the linear regression equation. The linear regression equation determines the IC_{50} value in ethanoicl extract of parijoto fruit.

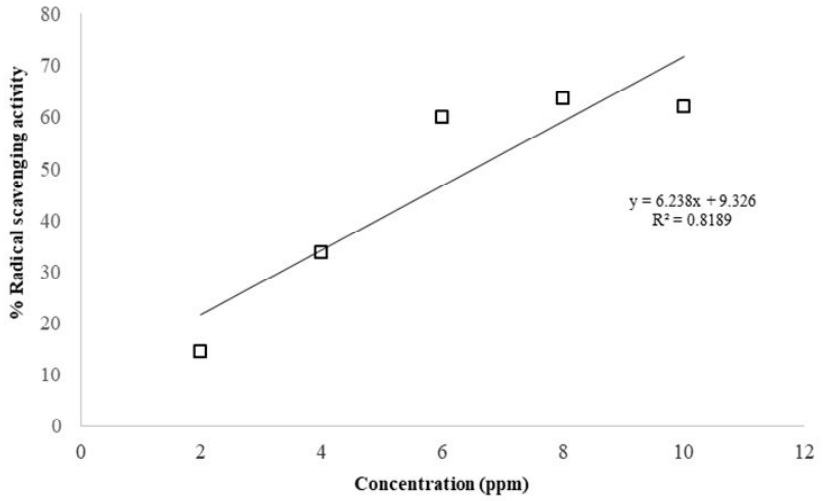

Figure 2. Correlation between radical scavenging activity and concentration of parijoto exctract

3.4. Radical scavenger activity of parijoto fruit fractions

Antioxidant testing was continued at the ethanol, ethyl acetate, and n-hexane fractions using the same method. In this test, $ABTS^{\cdot+}$ acts as a source of free radicals, while the Parijoto fractions act as a source of antioxidants that will reduce the presence of these radicals. The ethanolic fraction has an IC_{50} value of 3,874 ppm with a very strong antioxidant category as shown in Table 5.

Tabel 5. Antioxidant activity of parjoto ethanolic fraction

Concentration (ppm)	Abs	% Inhibition	IC_{50} (ppm)	Category
2	0.379	45.72		
4	0.357	46.12		
6	0.307	53.58	3.874	Very strong
8	0.141	78.65		
10	0.098	85.2		

The antioxidant activity of the parijoto ethyl acetate fraction in Table 6 shows that the ethyl acetate fraction can inhibit radicals with a stronger effectiveness than the n-hexane fraction. The ethyl acetate fraction produced antioxidant activity with IC_{50} values of 4,246 ppm and the antioxidant category was very strong. The difference in antioxidant activity produced by the two fractions is possible due to the influence of the polarity of the active compound on the fruit of Parijoto.

Tabel 6. Antioxidant activity of parijoto ethyl acetate fraction

Concentration (ppm)	Abs	% Inhibition	IC_{50} (ppm)	Category
2	0.343	34.17		
4	0.273	47.60		
6	0.184	64.62	4.246	Very strong
8	0.127	75.56		
10	0.083	84.13		

Antioxidant activity have correlation to the amount and composition of active compounds in a natural substance. The content and properties of active compounds in a natural material also affect its bioactivity. The antioxidant test of the parijoto n-hexane fraction shown in Table 7 gives lower results compared to the extract and the other two fractions. IC_{50} value of n-hexane fraction was 118.424 ppm with moderate antioxidant category.

Tabel 7. Antioxidant activity of parijoto n-hexane fraction

Concentration (ppm)	Abs	% Inhibition	IC_{50} (ppm)	Category
2	0.41	33.71		
4	0.39	36.89		
6	0.386	37.49	118.424	Medium
8	0.384	36.46		
10	0.401	35.17		

IC_{50} is an antioxidant concentration that can reduce 50% of free radicals. IC_{50} values in the parijoto fractions were determined in the same way through a linear regression equation. IC_{50}values of the ethanol and ethyl acetate fractions are included in the category of very strong antioxidants, meaning that at very small concentrations the ethanol and ethyl acetate fractions are able to inhibit the formation of free radicals. The graph of the relationship between the value of inhibition (free radical scavenger) and the concentrations of ethanol and ethyl acetate of parijoto fruit is shown in Figure 3 and 4. The increase in concentration in both fractions is in line with the increase in its radical inhibitory activity.

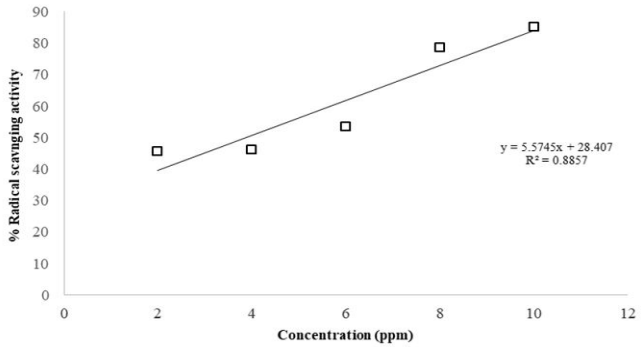

Figure 3. Correlation between radical scavenging activity and concentration of parijoto ethanolic fraction

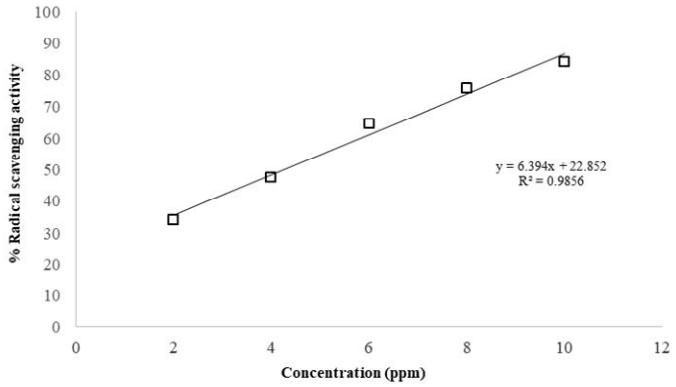

Figure 4. Correlation between radical scavenging activity and concentration of parijoto ethyl acetate fraction

Different results are shown by the antioxidant activity of the parijoto n-hexane fraction in Figure 5. The IC_{50} value produced by the n-hexane fraction is weaker than the ethyl acetate and ethanol fractions of the parijoto fruit. Active compounds that are attracted to n-hexane solvents tend to be non-polar. Polarity of the compound influences the antioxidant activity produced. The compounds that are thought to have antioxidant effects on parijoto are flavonoids, tannins, anthocyanins, and glycosides [7]. Most of these compounds are polar to semi-polar. The n-hexane fraction produces less optimal inhibitory activity because the active antioxidant potential of parijoto fruit is not completely attracted through non-polar solvents.

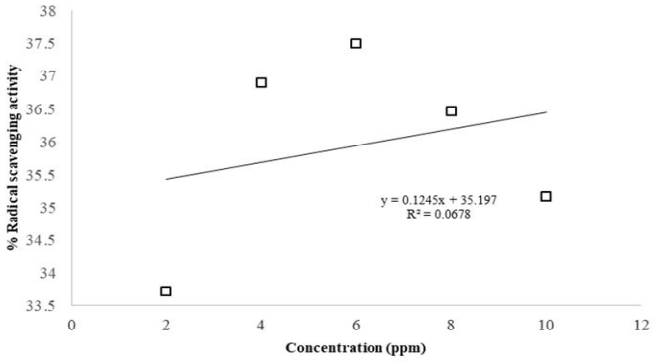

Figure 5. Correlation between radical scavenger activity and concentration of parijoto n-hexane fraction

Determining of antioxidant activity using ABTS method is very effective, simple, flexible, and easily repeated. ABTS is a radical with a nitrogen center with greenish-blue characteristics and when reduced by antioxidants to a colorless, non-radical form. The color change is due to the donation of hydrogen atoms from antioxidants to ABTS radicals [12, 20]. The principle of testing with this method is to measure the relative ability of antioxidants to reduce ABTS free radicals [19].

The secondary metabolite compounds in a natural material determine its bioactivity. Flavonoids are one of the phenolic compounds in natural materials that play an important role as neutralizers. Flavonoids have the potential as antioxidants and chelating metals. The antioxidant effect on flavonoids is closely related to its activities as anti-inflammatory, antiviral, anti-carcinogenic, hypo-

allergenic, and hepatoprotective [21]. The flavonoids contained in parijoto fruit have an excellent radical antidote activity, so they can be further developed as candidates for natural antioxidants.

4. Conclusion

Ethanol 96% solvent yields a more optimal yield with a yield of 18.5%. Testing the antioxidant activity of ethanol extract and parijoto fractions shows that the extract and fractions of parijoto fruit have antioxidant activity. The ethanol fraction of Parijoto has the best antioxidant activity compared to the extract and the two other fractions. IC50 value of ethanol fraction of 3,874 ppm with a very strong category of antioxidants.

Acknowledgements

I wish to express gratitude to the Institute of Research and Community Service at Ngudi Waluyo University for providing material support in the form of Internal DIPA funding in 2018 so that this research can be carried out well.

References

[1] Ansari, A. Q., Ahmed, S. A., Waheed, M. A., & Juned, S. (2013). Extraction and determination of antioxidant activity of *Withania somnifera* Dunal. *Eur J Exp Biol*, 3(5), 502-507.

[2] Rakesh, S. U., Patil, P. R., & Mane, S. R. (2010). Use of natural antioxidants to scavenge free radicals: a major cause of diseases. *International Journal of PharmTech Research*, 2(2), 1074-1081.

[3] Kapadiya, D. B., Dabhi, B. K., & Aparnathi, K. D. (2016). Spices and herbs as a source of natural antioxidants for food. *International Journal of Current Microbiology and Applied Sciences*, 5(7), 280-8.

[4] Widianingsih, M. (2017). Aktivitas Antioksidan Ekstrak Metanol Buah Naga Merah (*Hylocereus polyrhizus* (FAC Weber) Britton & Rose) Hasil Maserasi dan dipekatkan dengan Kering Angin. *Jurnal Wiyata Penelitian Sains dan Kesehatan*, 3(2), 146-150.

[5] Fernandes, R. D. P. P., Trindade, M. A., Tonin, F. G., Lima, C. G. D., Pugine, S. M. P., Munekata, P. E. S., & De Melo, M. P. (2016). Evaluation of antioxidant capacity of 13 plant extracts by three different methods: cluster analyses applied for selection of the natural extracts with higher antioxidant capacity to replace synthetic antioxidant in lamb burgers. *Journal of food science and technology*, 53(1), 451-460.

[6] Galvez, M. A. C. (2015). Evaluation of DPPH Free Radical Scavenging Activity and Phytochemical Screening of Selected Folkloric Medicinal Plants in Tinoc, Ifugao, Cordillera Administrative Region, Philippines. *International Journal of Scientific and Research Publications,* 5(12), 440-445.

[7] Vifta, R. L., & Advistasari, Y. D. (2018). Skrining Fitokimia, Karakterisasi, dan Penentuan Kadar Flavonoid Total Ekstrak dan Fraksi-Fraksi Buah Parijoto (*Medinilla speciosa* B.). In *Prosiding Seminar Nasional Unimus* (Vol. 1).

[8] Loganayaki, N., Siddhuraju, P., & Manian, S. (2013). Antioxidant activity and free radical scavenging capacity of phenolic extracts from *Helicteres isora* L. and *Ceiba pentandra* L. *Journal of food science and technology*, 50(4), 687-695.

[9] Maesaroh, K., Kurnia, D., & Al Anshori, J. (2018). Perbandingan Metode Uji Aktivitas Antioksidan DPPH, FRAP dan FIC Terhadap Asam Askorbat, Asam Galat dan Kuersetin. *Chimica et Natura Acta*, 6(2), 93-100.

[10] Floegel, A., Kim, D. O., Chung, S. J., Koo, S. I., & Chun, O. K. (2011). Comparison of ABTS/DPPH assays to measure antioxidant capacity in popular antioxidant-rich US foods. *Journal of food composition and analysis*, 24(7), 1043-1048.

[11] Shalaby, E. A., & Shanab, S. M. (2013). Comparison of DPPH and ABTS assays for determining antioxidant potential of water and methanol extracts of *Spirulina platensis*. *Indian Journal of Geo-Marine Sciences* 42(5):556-56

[12] Zheng, L., Zhao, M., Xiao, C., Zhao, Q., & Su, G. (2016). Practical problems when using ABTS assay to assess the radical-scavenging activity of peptides: Importance of controlling reaction pH and time. *Food chemistry*, 192, 288-294.
[13] Kumar, S., Jyotirmayee, K., & Sarangi, M. (2013). Thin layer chromatography: a tool of biotechnology for isolation of bioactive compounds from medicinal plants. *International Journal of Pharmaceutical Sciences Review and Research*, 18(1), 126-132.
[14] Arifianti, L., Oktarina, R. D., & Kusumawati, I. (2014). Pengaruh jenis pelarut pengektraksi terhadap kadar sinensetin dalam ekstrak daun *Orthosiphon stamineus* Benth. *E-Journal Planta Husada*, 2(1), 1-4.
[15] Senja, R. Y., Issusilaningtyas, E., Nugroho, A. K., & Setyowati, E. P. (2014). The comparison of extraction method and solvent variation on yield and antioxidant activity of *Brassica oleracea* l. Var. Capitata f. Rubra extract. *Majalah Obat Tradisional (Traditional Medicine Journal)*, 19(1), 43-48.
[16] Luís, Â., Neiva, D. M., Pereira, H., Gominho, J., Domingues, F., & Duarte, A. P. (2016). Bioassay-guided fractionation, GC–MS identification and in vitro evaluation of antioxidant and antimicrobial activities of bioactive compounds from *Eucalyptus globulus* stump wood methanolic extract. *Industrial Crops and Products*, 91, 97-103.
[17] Gullón, B., Lú-Chau, T. A., Moreira, M. T., Lema, J. M., & Eibes, G. (2017). Rutin: A review on extraction, identification and purification methods, biological activities and approaches to enhance its bioavailability. *Trends in food science & technology*, 67, 220-235.
[18] Preethi, J., Harita, B., & Rajesh, T. (2017). Review on Thin Layer Chromatography. *Journal of Formulation Science and Bioavailability*, 1, 107.
[19] Gwatidzo, L., Dzomba, P., & Mangena, M. (2018). TLC separation and antioxidant activity of flavonoids from *Carissa bispinosa, Ficus sycomorus*, and *Grewia bicolar* fruits. *Nutrire*, 43(1), 3.
[20] Fitriana, W. D., Ersam, T., Shimizu, K., & Fatmawati, S. (2016). Antioxidant activity of *Moringa oleifera* extracts. *Indonesian Journal of Chemistry*, 16(3), 297-301.
[21] Sarian, M. N., Ahmed, Q. U., So'ad, M., Zaiton, S., Alhassan, A. M., Murugesu, S., & Latip, J. (2017). Antioxidant and antidiabetic effects of flavonoids: A structure-activity relationship based study. *BioMed research international*, 2017.

Hydrogen bonding investigation of poly(3-hydroxybutyrate) / glycol chitosan blends studied by infrared and terahertz spectroscopies

Dian Marlina[1,2], Harumi Sato[1]

[1]Graduate School of Human Development and Environment, Kobe University, Tsurukabuto Nada-ku, Kobe 657–8501, Japan

[2]Faculty of Pharmacy, Universitas Setia Budi, Jl. Letjend Sutoyo Mojosongo Solo, Central Java 57127, Indonesia

hsato@tiger.kobe-u.ac.jp

Abstract. Poly(3-hydroxybutyrate) (PHB)/glycol chitosan (GC) polymer blend was developed as one of the new biopolymer materials. Effects of different PHB / GC concentrations were analysed as a function of the blend compositions by using Fourier transform infrared (FTIR) and terahertz (THz) spectroscopies to investigate the changes in the higher-order structure and bonding of hydrogen. The higher-order structure and hydrogen bonding monitored in this study include the crystalline structure and (C=O···H-C) hydrogen bonding of PHB. The FTIR and THz spectra showed that PHB's higher-order structure transforms into the less-order structure by adding GC without altering the crystalline structure and PHB's intramolecular (C = O ... H-C) hydrogen bonding with increasing GC concentration. Because of the addition of GC, the intensity ratio of THz bands figure out the crystalline dynamics of PHB, the helical structure deformation occurs first followed by the weakening of intramolecular (C = O ... H-C) hydrogen bonding within PHB-PHB molecules.

Keywords: Chitosan, higher-order structure, hydrogen bonding, low-frequency vibrational spectroscopy

1. Introduction

Polymers are now available in tremendous quantity and variety of materials to accommodate the needs of modern society. They can be produced in numerous applications such as energy, information technology, medical, living, and environment. However, most of them are made from traditional petroleum derivatives that cannot be decomposed in natural environment leading to major earth-environmental pollution problem [1,2]. The excessive usage of these fuel-based polymeric materials will also result in the depletion of unrenewable petroleum resources [3]. As a result, development of new biopolymers, polymers of biological origin are expected as a material to replace petroleum-based polymers. Biopolymer is characterized by biocompatibility, biodegradability, and adsorptive ability that is suitable for the application in contact with living organisms [4].

Bacteria synthesized poly(3-hydroxybutyrate) or PHB is the most known biopolymer from polyhydroxyalkanoates (PHAs) family; it is a linier polyester of biological origin (Figure 1a). Its

biodegradability and biocompatibility make PHB in high demand for wide-range of utilizations. However, the potential applications of PHB are limited by its physical properties; PHB shows high crystalline feature and narrow processing thermal condition [5,6]. Therefore, the modification of PHB is needed to improve those properties. Here, we have modified PHB by blending technique with glycol chitosan or GC (Figure 1b). It is a polysaccharide chitosan derivative which enhanced water solubility. GC also has biodegradable and biocompatible properties; thus PHB/GC will result as a fully biodegradable PHB-based polymer system [7].

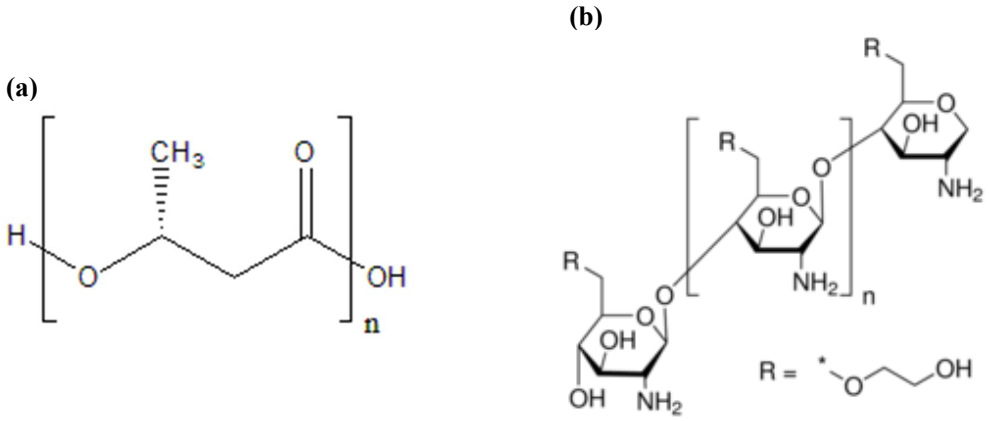

Figure 1. (a) Chemical structure of poly(3-hydroxybutyrate) (PHB) and (b) glycol chitosan (GC).

Hydrogen bonding is expected to play an important role in stabilizing the higher-order structure of polymers. Previous differential scanning calorimetry (DSC), X-ray, infrared, and Raman studies have reported the existence of weak (C=O···H-C) hydrogen bonding interaction (around 5 $kJmol^{-1}$) between C=O and CH_3 groups in the crystalline structure of PHB [5,6,8,9]. Information related to this hydrogen bonding can also be observed directly in the low-frequency region (3.3–330 cm^{-1}) using terahertz (THz) spectroscopy. Since low-frequency vibrational spectra are derived from intra and intermolecular interactions, THz spectroscopy can be powerful tool to reveal the formation of higher-order structures of not only homopolymer but also modified polymer. The investigation of homopolymer PHB, PHB-based copolymer and PHB-based polymer blend systems; poly(3-hydroxybutyrate-*co*-3-hydroxyvalerate) (P(HB-*co*-HV)) and PHB/poly(4-vinylphenol) (PVPh) by using low-frequency vibrational spectroscopy have been successfully performed in the previous study [10-14]. By investigate temperature, polarized dependence together with quantum chemical calculation, the bands appeared in the region 120–70 cm^{-1} of THz spectra was assigned to vibrational motion of (C=O···H-C) hydrogen bonding of PHB [10-12]. The study of (P(HB-*co*-HV)) successfully reported the crystalline structure change from PHB-type structure to PHV-type, as shown in the infrared and X-ray studies [13,15]. PHB/PVPh study progressively reported the formation of new peak due to intermolecular hydrogen bonding between PHB and PVPh molecules [14]. In this study we attempted to elucidate the change in the higher-order structure and hydrogen bonding formed by polymer blends of PHB and glycol chitosan.

2. Methods

2.1. Materials and sample preparation

Low-molecular weight PHB (MW ~1000) was supplied from Polysciences, Inc. and glycol chitosan (purity ≥ 60%, degree of deacetylation = 91.6%) [16] was purchased from Sigma-Aldrich Co., they were used as received without any purification process. 1,1,1,3,3,3-Hexafluoro-2-propanol (HFIP) was supplied by Wako Pure Chemical Industries, Ltd. Samples of PHB/GC blends were prepared by dissolving PHB and glycol chitosan in HFIP with prescribed weight percentage. The films were prepared

by pouring the solution of blend samples on an aluminium dish, followed by evaporation at 20℃, and then continued by drying in a vacuum oven at 70℃ for 12h.

2.2. Measurements

A Thermo Nicolet Nexus 470 FTIR equipped with a liquid nitrogen cooled system and a mercury cadmium telluride (MCT) detector was used to perform Fourier transform infrared (FTIR) spectra of the PHB / GC blend films. The measurements were performed using Microm ATR with 128 scans at a 2 cm^{-1} resolutions. On the other hand, THz spectra of the blend films were measured by using a terahertz time-domain spectrometer (THz-TDS), TAS7400TS from ADVANTEST Co. The spectra were obtained in the transmission mode in the 120–60 cm^{-1}region with 1024 scans and 0.25 cm^{-1} spectral resolution.

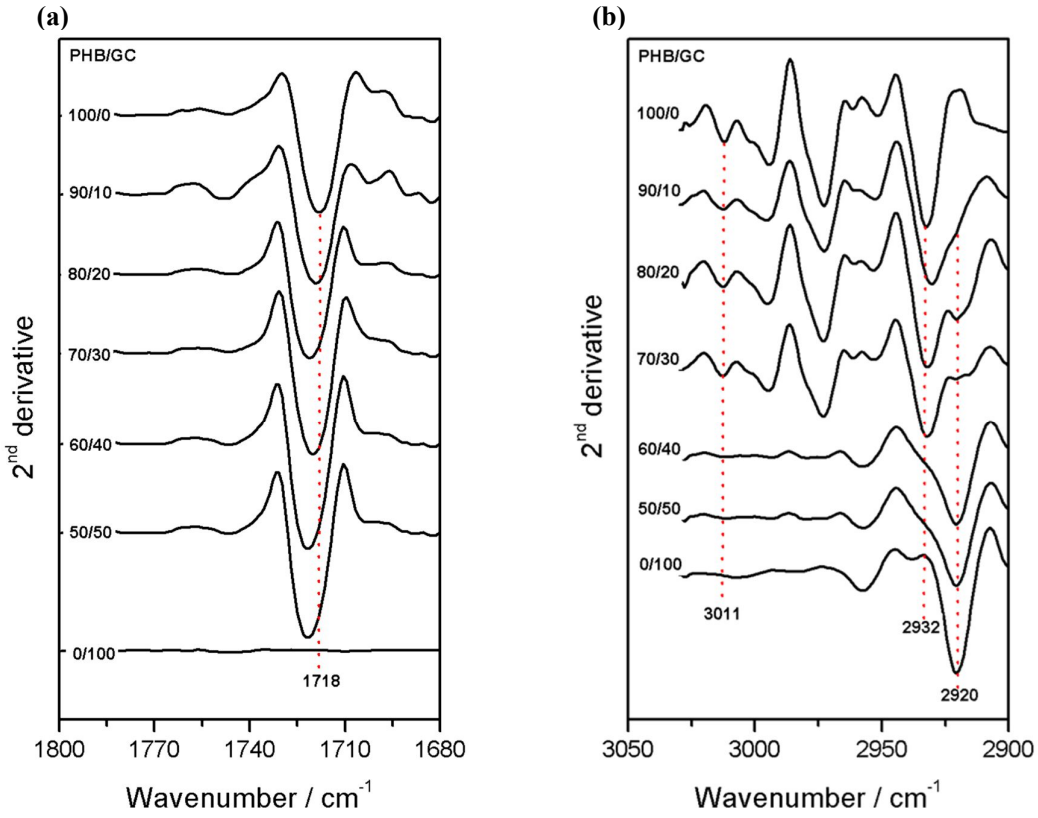

Figure 2. Second derivative FTIR spectra of PHB/GC with various blending ratios in the (a) C=O stretching and (b) C-H stretching region.

3. Results and discussion

3.1. Composition-dependent spectra in the C=O stretching and C-H stretching region

Figure 2 shows the second derivative FTIR spectra obtained at room temperature for the film samples of pure PHB, PHB/GC blends with increasing GC concentrations, and pure GC; (100/0), (90/10), (80/20), (70/0), (60/40), (50/50), and (0/100) in the C=O stretching and C-H stretching region. In the region of 1800–1680 cm^{-1}, PHB shows a sharp band centred at 1718 cm^{-1} due to C=O stretching mode of PHB in the crystalline state [5]. This band refer to intramolecular (C=O···H-C) hydrogen bonding interaction between C=O group in one helix and the CH_3 group in another helix of PHB molecules [6]. On the other

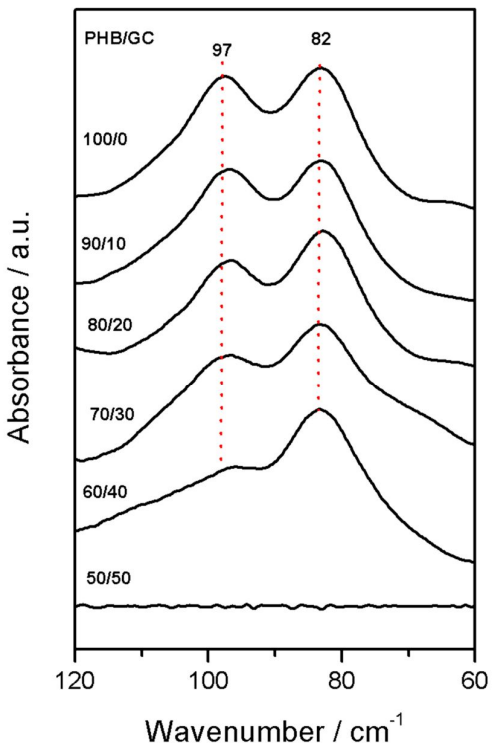

Figure 3. THz spectra of PHB/GC with various blending ratios.

hand, pure GC does not any show any band since there is no carbonyl group in its chemical structure (Figure 1(b)).

In Figure 2a, position of the band related to the intramolecular C=O gradually shifts to the higher wavenumber from 1718 to 1724 cm^{-1} with increasing the GC concentrations in the blends. It indicates that the intramolecular (C=O ··· H-C) hydrogen bonding of PHB weaken by the addition of GC. A band appears at 3011cm^{-1} in the C-H stretching region (Figure 2b) has been assigned to the C-H stretching mode of the (C=O ··· H-C) hydrogen bonding of the PHB higher-order structure [5]. The band at 3011 cm^{-1} gradually decreases with increasing GC concentration in the blends from PHB/GC (100/0), (90/10), (80/20), (70/0) and completely disappears when PHB ≤ 60%, indicating that the higher-order structure of PHB is destructed by the addition of GC. Therefore, when the concentration of GC increases, the development of higher-order structure of PHB becomes difficult in these blend samples. This band's location does not change with that concentration of GC relative to pure PHB, it explains the PHB's crystalline structure does not change through mixing with GC.

3.2. Composition-dependent THz spectra of PHB/GC

Figure 3 shows the THz spectra of pure PHB and PHB/GC blends with increasing the GC concentrations in the region of 120–60 cm^{-1} collected at room temperature. They are two bands centred at 97 and 82 cm^{-1}. The band at 97 cm^{-1} was assigned to the out-of-plane CH_2 and CH_3 vibrations which directed to spring like motion of helical structure. On the other hand, the band at 82 cm^{-1} was assigned to the out of plane C=O and CH_3 vibrations which directly reflect the intramolecular (C=O···H-C) hydrogen bonding of PHB crystalline state [12].

The absorbance of the bands at 97 and 82 cm^{-1} gradually decreases with increasing GC concentration in the blends from PHB/GC (100/0), (90/10), (80/20), (70/30) to (60/40) and completely disappear in the PHB/GC (50/50). Plots of the absorbance of these bands versus PHB concentrations can be seen in Figure 4a. In detail, the reduction of the band at 97 cm^{-1} reveals the transformation of PHB helical structure from the higher-order to less-order structure. While the reduction of the band at 82 cm^{-1} indicates that the intramolecular (C=O···H-C) hydrogen bonding within PHB weaken with increasing GC concentration. However, the position of these bands does not show any significant change with variation in the blend concentration means there is no change in the crystalline structure of PHB. It is consistent with the higher-frequency vibrational region results. The crystalline dynamics of PHB/GC can also be figured out by exploring the change of PHB intensity ratio due to the blends. In the Figure 4b, it is clear that the intensity ratio of the two bands at 97 and 82 cm^{-1} gradually decreases with reduction of the PHB concentration. It indicates that the deformation of helical structure happens first followed by the weakening of intramolecular (C=O···H-C) hydrogen bonding within PHB-PHB molecules.

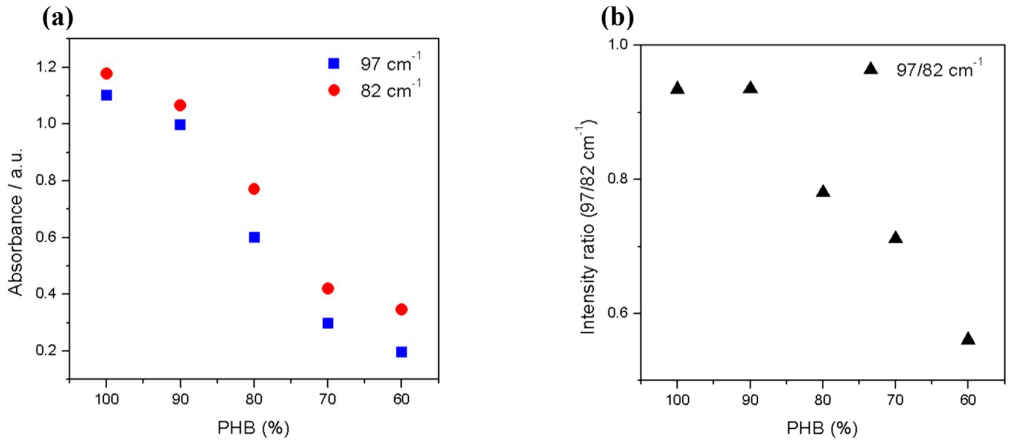

Figure 4. (a) Plots of absorbance and (b) intensity ratio of the bands at 97 and 82cm^{-1} relative to PHB concentrations.

4. Conclusion

The change in the higher-order structure and hydrogen bonding formed by polymer blends of PHB and glycol chitosan with various blending concentration has been investigated by FTIR and THz spectroscopies. Through introducing glycol chitosan to the PHB, FTIR spectra revealed the band's lower wavenumber changes at 1718 cm^{-1} as a result on the weakening of intramolecular (C=O···H-C) hydrogen bonding between PHB-PHB molecules. In contrast, the 3011 cm^{-1} band reduces and disappears completely once PHB ≤ 60%, suggesting that PHB's higher-order structure is disrupted by the introduction of GC. THz spectra showed band reduction at 97 and 82 cm^{-1} suggests that higher-order PHB structure transforms into lower-order structure and intramolecular (C=O···H-C) hydrogen bonding within PHB weakened with increasing concentration of GC, respectively. The frequency ratio of THz bands revealed that helical structure deformation occurs first, followed by the weakening of intramolecular (C=O···H-C) hydrogen bonding between PHB-PHB molecules.

References

[1] Derraik, J. G. (2002). The pollution of the marine environment by plastic debris: a review. Marine pollution bulletin, 44(9), 842-852.

[2] Rios, L. M., Moore, C., & Jones, P. R. (2007). Persistent organic pollutants carried by synthetic polymers in the ocean environment. Marine Pollution Bulletin, 54(8), 1230-1237.

[3] Sorrell, S., Speirs, J., Bentley, R., Brandt, A., & Miller, R. (2010). Global oil depletion: A review of the evidence. Energy Policy, 38(9), 5290-5295.

[4] Shchipunov, Y. (2012). Bionanocomposites: Green sustainable materials for the near future. Pure and Applied Chemistry, 84(12), 2579-2607.

[5] Sato, H., Murakami, R., Padermshoke, A., Hirose, F., Senda, K., Noda, I., & Ozaki, Y. (2004). Infrared Spectroscopy Studies of CH⊙⊙⊙ O Hydrogen Bondings and Thermal Behavior of Biodegradable Poly (hydroxyalkanoate). Macromolecules, 37(19), 7203-7213.

[6] Sato, H., Mori, K., Murakami, R., Ando, Y., Takahashi, I., Zhang, J., ... & Noda, I. (2006). Crystal and Lamella Structure and C− H⊙⊙⊙ OC Hydrogen Bonding of Poly (3-hydroxyalkanoate) Studied by X-ray Diffraction and Infrared Spectroscopy. Macromolecules, 39(4), 1525-1531.

[7] Nam, H. Y., Kwon, S. M., Chung, H., Lee, S. Y., Kwon, S. H., Jeon, H., ... & Oh, Y. K. (2009). Cellular uptake mechanism and intracellular fate of hydrophobically modified glycol chitosan nanoparticles. Journal of Controlled Release, 135(3), 259-267.

[8] Sato, H., Ando, Y., Dybal, J., Iwata, T., Noda, I., & Ozaki, Y. (2008). Crystal structures, thermal behaviors, and CH center dot center dot center dot O= C hydrogen bondings of poly (3-

hydroxyvalerate) and poly (3-hydroxybutyrate) studied by infrared spectroscopy and X-ray diffraction. Macromolecules, 41(12), 4305-4312.

[9] Sato, H., Murakami, R., Noda, I., & Ozaki, Y. (2005). Infrared and Raman spectroscopy and quantum chemistry calculation studies of C–H··· O hydrogen bondings and thermal behavior of biodegradable polyhydroxyalkanoate. Journal of molecular structure, 744, 35-46.

[10] Hoshina, H., Morisawa, Y., Sato, H., Kamiya, A., Noda, I., Ozaki, Y., & Otani, C. (2010). Higher order conformation of poly (3-hydroxyalkanoates) studied by terahertz time-domain spectroscopy. Applied Physics Letters, 96(10), 101904.

[11] Hoshina, H., Morisawa, Y., Sato, H., Minamide, H., Noda, I., Ozaki, Y., & Otani, C. (2011). Polarization and temperature dependent spectra of poly (3-hydroxyalkanoate) s measured at terahertz frequencies. Physical Chemistry Chemical Physics, 13(20), 9173-9179.

[12] Yamamoto, S., Morisawa, Y., Sato, H., Hoshina, H., & Ozaki, Y. (2013). Quantum mechanical interpretation of intermolecular vibrational modes of crystalline poly-(r)-3-hydroxybutyrate observed in low-frequency raman and terahertz spectra. The Journal of Physical Chemistry B, 117(7), 2180-2187.

[13] Marlina, D., Sato, H., Hoshina, H., & Ozaki, Y. (2018). Intermolecular interactions of poly (3-hydroxybutyrate-co-3-hydroxyvalerate)(P (HB-co-HV)) with PHB-type crystal structure and PHV-type crystal structure studied by low-frequency Raman and terahertz spectroscopy. Polymer, 135, 331-337.

[14] Marlina, D., Hoshina, H., Ozaki, Y., & Sato, H. (2019). Crystallization and crystalline dynamics of poly (3-hydroxybutyrate)/poly (4-vinylphenol) polymer blends studied by low-frequency vibrational spectroscopy. Polymer, 121790.

[15] Sato, H., Ando, Y., Mitomo, H., & Ozaki, Y. (2011). Infrared spectroscopy and X-ray diffraction studies of thermal behavior and lamella structures of poly (3-hydroxybutyrate-co-3-hydroxyvalerate)(P (HB-co-HV)) with PHB-type crystal structure and PHV-type crystal structure. Macromolecules, 44(8), 2829-2837.

[16] Lavertu, M., Xia, Z., Serreqi, A. N., Berrada, M., Rodrigues, A., Wang, D., ... & Gupta, A. (2003). A validated 1H NMR method for the determination of the degree of deacetylation of chitosan. Journal of pharmaceutical and biomedical analysis, 32(6), 1149-1158.

Bioconversion on Wastewater of Soybeans using Microbial Fuel Cell

Yohanes A Cahyono, Tilana Madurani, Widya F Azzahra, Retno A S Lestari

Chemical Engineering Department, University of 17 Agustus 1945 Semarang

retnotengaran@gmail.com

Abstract. Microbial fuel cell (MFC) is a technology developed to obtain new sources of renewable energy to produce electricity. It can be an alternative for wastewater treatment and bioenergy producers of renewable electricity. This method requires bacteria to convert substrate in wastewater into electrical energy. The mechanism of MFC were oxidation of substrate by bacteria to produce electrons and protons at the anode. The proton in anode chamber passes through a membrane exchange to the cathode chamber, however the electrons couldn't through. It caused accumulation of electron in anode chamber and then both of electrode had a potential difference, so electron in anode chamber passed through membrane exchange to cathode chamber. In this study used dual-chambers reactors with each compartment having 8 cm × 10 cm × 10 cm of dimensions and 5 mm of thickness. This study was subjected to evaluate the performance of MFC in soybean washing wastewater treatment with bacteria of EM4 to analyze the potentials production of electricity energy. The focus of this study was to evaluate the effect of time to electricity. MFC system was observed for 40 hours, measurement of voltages and electric currents performed every 4 hours. The results showed that there was potential of electricity production from soybean wastewater treatment by MFC. The maximum electricity reached in soybean wastewater media were voltage 441 mV (at 24 h), the electric currents 170 μA and the power density 51, 35 mW/m2 (at 24 h after acclimatization). Increasing of time effect to decreasing of electricity produced.

Keywords: bioenergy, electricity, microbial fuel cell, membrane, wastewater soybean

1. Introduction

One of the renewable alternative energy to produce electricity is Fuel Cell (FC), which produces energy by using High Value Metal Catalyst. FC have advantages over other energy because FC was not produce exhaust emissions such as SOx, NOx, CO2, and CO, and has high efficiency [1]. One such of FC used active microbes as biocatalysts in anaerobic anode chambers to produce biolytic known as Microbial Fuel Cell (MFC) [2]. MFC utilize microbial as a biocatalyst and capture the electricity from an organic and inorganic substances through the activity of microbial [3]. In MFC there are two anode and cathode chambers, the anode chamber set in anaerobic condition but in the cathode chamber, oxygen allowed to circulate and contains an electrolyte solution as an electron acceptor. In MFCs, microorganisms employ a solid electrode in an anode as the terminal electron acceptor of their electroactive anaerobic [4]. Through the metabolic activity of anaerobic microorganisms convert organic matter to be electricity [5,6]. Oxidation-reduction reactions occur in the microbial electrochemical systems through two steps.

The first, microbial in the anode interaction is initiated to oxidize the organic substrate into smaller organic molecules, protons, electron and carbon dioxide [3]. The second, electron transfering from the anode to the cathode through the external electrical circuit, and the protons into anode transferred to chatode by membrane. In the chatode proton and electron react to form water and bioelectric current detected because there are electron flow through the external circuit. Electrolyte electron acceptors in cathode act as electron catchers. One such of electron acceptor electrolyte is potassium ferricyanide ($K_3Fe(CN)_6$). The reaction is as follows:

$$4\ Fe(CN)_6^{3-} + 4e^- \rightarrow 4\ Fe(CN)_6^{4-} \quad (1)$$

$$4\ Fe(CN)_6^{4-} + 4H^+ + O_2 \rightarrow 4\ Fe(CN)_6^{3-} + 2H_2O \quad (2)$$

The long-term performance of ferricyanide in the MFC system is strongly influenced by the efficiency of its diffusion through PEM to the cathode chamber [11].

2. Methods

2.1. Material and Equipment Preparation

The equipment of MFC using dual chambers were made up of glass sheet material with working volume "800 ml" for each chamber, with dimension 8 cm × 10 cm × 10 cm and 5 mm of thickness. Anode and chatode chamber were separated by proton exchange membrane (type Nafion 117) and connected by electrode. Carbon coated on carbon cloth acts as anode electrode, while platinum/C coated on carbon cloth acts as cathode electrode. The compartment configuration of microbial fuel cell, with wastewater soybeans substrate is shown in Figure 1. Before being applied to MFC, PEM was sterilized used aquadest at "100°C" for 1 hour then heated in 3% hydrogen peroxide for 1 hour then rinsed by water, next heated in 1M sulfuric acid for 1 hour. This process to clean the pores of PEM from contaminants. The microbial fuel cell equipment was sterilized by cleaned and rinsed with 70% ethanol to remove the bacterial.

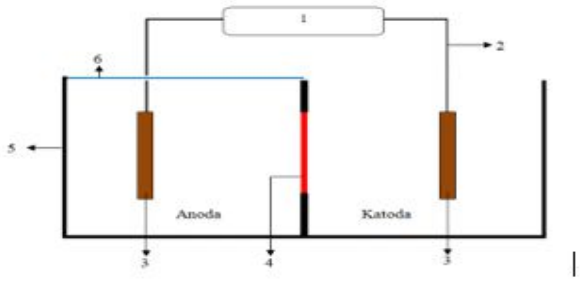

1. Measuring instrument, 2. Power Cable, 3. Electrode, 4. Proto Exchange Membrane (PEM), 5. Anode Chamber, 6. Cathode Chamber

Figure 1. Schematic Microbial Fuel Cell Dual Chamber

2.2. Bioelectricity Conversion

After all the equipment ready fill up the anode chamber with soybean wastewater as substrate and EM4 as bacteria source. The anode chamber maintained at pH 4.1 and sealed to keep anaerobic condition. 450 ml kalium permanganate was filled on chatode chamber which was worked on anaerobic condition. The anode and chatode electrode was connected by stainless steel wire (type 316).

3. Results and Discussion

3.1. The Effect of Optical Density to Voltage

Figure 2 shows that from the bioconversion process of organic matter of waste water soybeans in processing for the production of tempe using the MFC method could produce electricity. The electricity was produced of reforming nutrients in organic matter of wastewater soybeans by bacteria contained in EM4 which produced protons and electrons. These protons exchange to the cathode/anode and then reacts with $KMnO_4$ to produced H_2O. Based on Figure 2, it appears that for increasing of OD effect to increasing voltage of electricity, it caused the increasing of OD in substrate similar the amount of bacteria that change the substrate from the processing of soybean liquid waste.

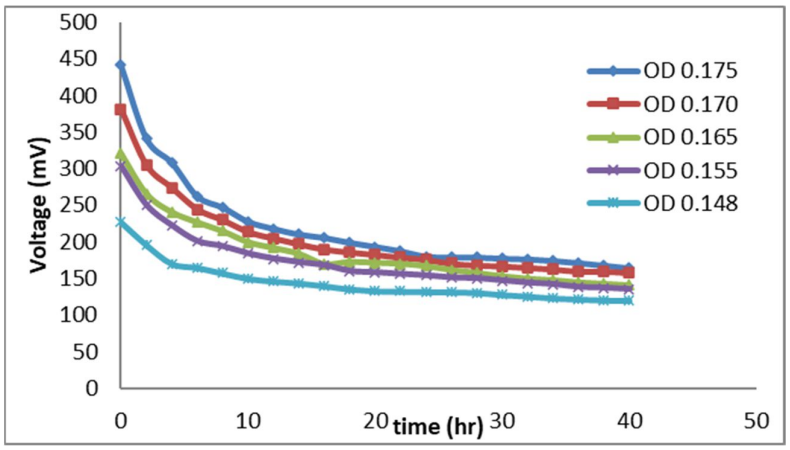

Figure 2. Time dependence to the Electrical Voltage

3.2. The Effect of Optical Density to Electrical Current

Figure 3 shows that increasing time makes the electrical current decrease. Similar to the voltage of electrical produced in figure 2, the decreasing of electrical current was related to the number of free electrons produced by these bacteria. Figure 3 also shows that OD effect to the voltage and the electrical current produced by MFC system. The OD in substrate 0.175, the early of electrical current 162 µ A. and decrease to be 65 µ A after 40 hours. When the OD 0.148 In the early process, the electrical current 100 µ A, and after 40 hours, electrical current to be 56 µ A.

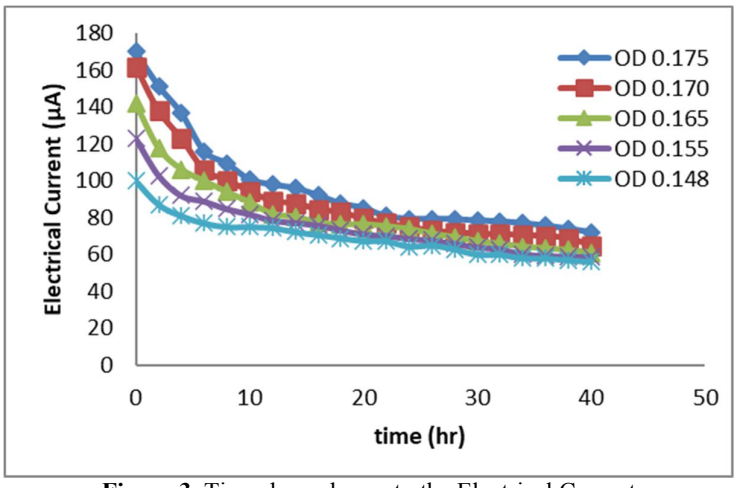

Figure 3. Time dependence to the Electrical Current

3.3. Power Density

The electrical current and voltage data from this study were treated with equation 3.1to get a power density value that can represent productionelectricity produced by the MFC system. The power density produced in this system is presented in Figure 4.

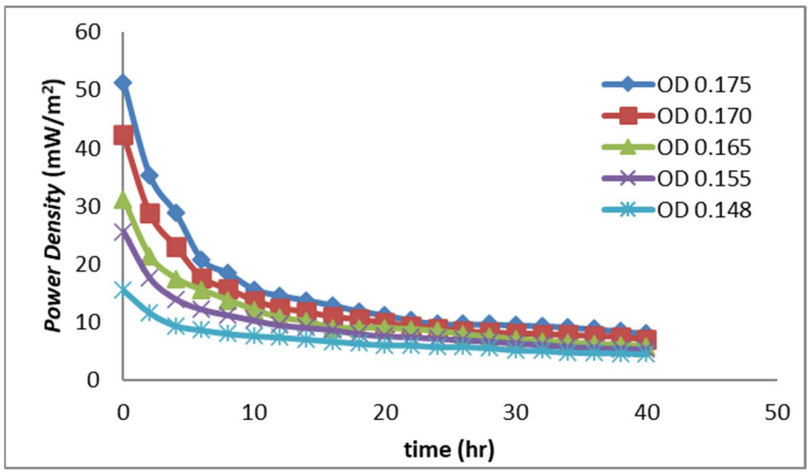

Figure 3. Time dependence to the Power Density

4. Conclusion

1. The bioconversion process of organic compound of waste water soybeans in processing for the production of tempe using the MFC method could produced electricity

2. The bioconversion process of organic compound of waste water soybeans in processing for the production of tempe using the MFC method could produced electricity

3. The increasing OD effect to the increasing voltage and current of electricity.

4. In the early process, the OD of substrate 0.175 produced the electricity voltage 441 mV and electrical current 162 µ A. After 40 hours, voltage to be 164.2 mV and electrical current 65 µ A. For OD substrate 0.148, in early process produced the voltage 227.2 mV and the electrical current 100 µ A, after 40 hours, the voltage to be 120 mV electrical current to be 56 µ A.

Acknowledgements

The authors would like to give thanks and acknowledgement to Directorate General of Research, Technology and Higher Educations of Indonesia for financial support of this research through research grant of Program Kreativitas Mahasiswa Penelitian Eksakta 2019. We also thank you to Chemical Engineering Department and Faculty of Engineering, University of 17 Agustus 1945 Semarang.

References

[1] Peighambardoust SJ, Rowshanzamir S, Amjadi M. Review of the proton exchange membranes for fuel cell applications. International Journal of Hydrogen Energy. 2010; 35:9349-84.

[2] Tardast, A, M. Rahimnejad, G. Najafpour, A.A. Ghoreyshi,Zare.2012. Fabrication and operation of a novel membrane-lessmicrobial fuel cell as a bioelectricity generator, Int. J. Environ.Eng. 3. 1–5.

[3] Allen R. Microbial fuel-cells: electricity production from carbohydrates. ApplBiochemBiotechnol

1993;39(40):27–40
[4] Kumar A, Hsu LHH, Kavanagh P, BarriereF, Lens PNL,Lapinsonniere L, et al. The ins and outs of microorganism-electrode electron transfer reactions. Nat Rev Chem 2017;1.
[5] Rabaey K, Verstraete W. Microbial fuel cells: novelbiotechnology for energy generation. Trends Biotechnol2005;23:291e8.
[6] Logan BE, Hamelers B, Rozendal RA, Schrorder U, Keller J,Freguia S, et al. Microbial fuel cells: methodology andtechnology. Environ SciTechnol 2006;40:5181e92.
[7] Selim RYAHHMM, Kamal AM, Ali DMM. Bioelectrochemical systems formeasuring microbial cellular functions. Electroanalysis 2017;29(6):1498–505.
[8] Logan BE, Regan JM. Electricity-producing bacterial communities in microbialfuel cells. Trends Microbiol 2006;14(12):512–8.
[9] Liu Z, Liu J, Zhang S, Su Z. Study of operational performance and electricalresponse on mediator-less microbial fuel cells fed with carbon- and protein-rich substrates. BiochemEng J 2009;45:185–91.
[10] Logan,B.E., Hamelers B., Rozendal R., Schröder U., Keller J., Freguia S., Aelterman P., Verstraete W., Rabaey K., Microbial fuel cells: methodology and technology, EnvironmentalScience&Technology (2006),https://doi.org/10.1021/ es0605016.
[11] Logan, B. E. Hamelers. B., R. Rozendal, U. Schro¨der, J. Keller,SFreguia, P. Aelterman, W. Verstraete, K. Rabaey. 2006. Microbialfuel cells: methodology and technology. Environ. Sci. Technol.40 5181–5192.

ASSET

Advance Sustainable Science, Engineering, and Technology

Available online at: publication.upgris.ac.id/index.php/asset/

Vol 1, No 1 (2019)